Developing and Improving a Thermometallurgical Model for 22MnB5 Steel in a Roller Hearth Furnace

by

Boxuan Zhao

A thesis

presented to the University of Waterloo

in fulfillment of the

thesis requirement for the degree of

Master of Applied Science

in

Mechanical and Mechatronics Engineering

Waterloo, Ontario, Canada, 2022

Author's Declaration

This thesis consists of material all of which I authored or co-authored: see Statement of Contributions included in the thesis. This is a true copy of the thesis, including any required final revisions, as accepted by my examiners.

I understand that my thesis may be made electronically available to the public.

Statement of Contributions

The author acknowledges the contributions of others to the work done in this thesis as listed below:

1. Timothy Sipkens, the second author of my journal paper [1], contributed to the writing of Sec. 5.2, and provided general editorial advice.

2. Constantin Chiriac, from Ford Motor Company, provided the data for roller hearth furnace trial.

3. Siyu Wu, from university of Guelph, provided some muffle furnace heated samples for the ex-situ FTIR measurements discussed in Sec. 3.2.3.

Abstract

Ultra-high strength steel (UHSS) such as Al-Si coated 22MnB5 are commonly used in the hot forming die quenching (HFDQ) process to produce light-weight automotive parts while maintaining good crashworthiness. The steel blank is typically austenitized in a roller hearth furnace, according to independently set heating zones and other parameters such as roller speed and part spacing. Most often these parameters are chosen heuristically based on experience, resulting in sub-optimal efficiency and part quality. To improve process efficiency and ensure complete austenitization before forming, a complete thermal-metallurgical furnace model that predicts the blank heating profile and the austenitization progress inside a roller hearth furnace is needed.

This work introduces a framework for the furnace model, then evaluates three candidate austenitization submodels of different levels of complexity, including: a first order (F1) kinetics model, an Internal State Variable (ISV) model, and a phenomenological model. To address the drawbacks of conventional goodness-of-fit model derivation and evaluation method, the Bayesian model selection technique is introduced and used to evaluate the three candidates. This technique considers the uncertainties in the data, and the trade-off between model complexity and accuracy. Dilatometry data is used to calibrate the models and validate them. The selected austenitization submodel, ISV model, is integrated into the overall furnace model and its performance is validated using roller hearth furnace trials collected with instrumented blanks. The resultant coupled thermo-metallurgical furnace model provides a useful tool for researchers and industrial engineers to maximize production rate and ensure consistent part quality.

Acknowledgements

I would first like to thank my supervisor Professor Kyle Daun, he was the reason why I chose to do a Master's and one of the main reasons that I could finish this journey. Without his dedication, support, mentoring, I would have never made it this far. On top of all, he is a wonderful mentor who genuinely cared about all his students and their well-being. Thank you! I would also like to thank Tim Sipkens for generously helping with the project. My sincerest gratitude also goes to our industry sponsor, Dr. Constantin Chiriac from Ford. Thank you for all the support on this project.

I consider myself extremely fortunate to be working in this lab that feels like a big family. Thanks to everyone here that made it a loving experience. Thank you to Stephen for providing the good vibes, my only regret is Covid kept me from hanging out with you more, but the time we had pre-covid was awesome. Thank you to Fatima for all the emotional support. We are so similar in personality and can always relate to each other's anxieties. It was always fun to talk to you about the new C-Drama you watched or Chinese words you learned. You are a genuinely awesome person. Thank you to Cameron Klassen, who I collaborated with on many experiments. Your calm demeanor has always been something I looked up to. You are such a great researcher and have always been setting the bar high for me throughout these two years. Congrats on your hard-earned achievements and MASc degree. There are many others in the lab that I can't all list here, but everyone has been truly delightful to be around and has helped me in many ways. Thank you to everyone and wish you all the best in your future endeavors.

On a more personal note, I couldn't have made it without my best friend, Lang, who is also a brilliant researcher and recently finished his Master's. We've been friends for over 8 years, embarked on this tough grad study journey together and shared so much laughter and so many tears. Thank you for always being there for me when I'm stressed, which to you must have felt like every other day. I'm sure there are great things to come for both of us. To my dearest friend, Ian, who I've been with since undergrad. Thank you so much for all the support and the good times. You have been my emotional corner stone and the main reason why I've enjoyed university so much (even though you think I'm always whining, I did enjoy it). I wish you all the best as you continue your journey on grad study, I have all the faith in a brilliant mind like yourself! Big thank you to all my other friends who have supported me throughout the years. I've been so lucky to

have you all as company. Thank you to my girlfriend for always being there for me, through the ups and downs. I have doubted myself from time to time, but you have always believed in me.

Last but certainly not least, I would like to dedicate the following message to my parents. They have worked tirelessly to provide for me, supported me unconditionally and have asked for nothing in return but for me to chase my own dreams and live a fulfilling life. They are the most wonderful parents in the world.（感谢我平凡又伟大的父母，感谢你们把我培养成了一个正直且善良的人。你们为我奉献了太多，从始至终无条件地支持我，相信我，却从不求回报，只希望我去追求自己的梦想。我自小就钦佩着你们的勤劳和勇气，你们一直是我的榜样。希望你们能够多休息，多享受自己的人生。你们是全天下最棒的父母!）

Table of Contents

List of Figures

List of Tables

Nomenclature

Symbol	Unit	Definition
c_p	J/(kg·K)	Specific heat of USIBOR® 1500
$c_{p,eff}$	J/(kg·K)	Effective specific heat of USIBOR® 1500
T_{Ac1}	°C	Austenitization onset temperature under non-isothermal heating
T_{Ac3}	°C	Austenitization completion temperature under non-isothermal heating
Ms	°C	Initiation of martensite transformation
M_f	°C	Completion of martensite transformation
T_{Ae1}	°C	Austenitization onset temperature under equilibrium
T_{Ae3}	°C	Austenitization completion temperature under equilibrium
T_s	K	Blank surface temperature
T_{blank}	K	Blank temperature (assumed to be uniform, i.e., = T_s)
T_{surr}	K	Surrounding temperature
T_{amb}	K	Ambient temperature
ρ	kg/m^3	Density of USIBOR® 1500
Δh_γ	J/kg	Latent heat of austenitization
df_γ/dt	1/s	Rate of austenitization
Q_{conv}	W	Convection heat transfer rate
Q_{rad}	W	Radiation heat transfer rate
$\bar{h}_{top}/\bar{h}_{bot}$	W/(m^2·K)	Convection coefficient
A	m^2	Surface area of the blank, single side
L_c	m	Characteristic length
P	m	Perimeter of the blank
k_{air}	W/(m·K)	Thermal conductivity of air
T_{film}	°C	Film temperature
$\overline{Nu}$	-	Nusselt number
Ra	-	Rayleigh number
v_{air}	m^2/s	kinematic viscosity of air
α_{air}	m^2/s	thermal diffusivity of air
β	1/K	Volumetric expansion coefficient

σ	$W/(m^2 \cdot K^4)$	Stephen-Boltzmann constant
α	-	total absorptivity
ε	-	total emissivity
ε_λ	-	spectral emissivity
α_λ	-	spectral absorptivity
$E_{\lambda b}$	$W/(m^2 \cdot \mu m)$	spectral blackbody emissive power
E_b	W/m^2	total black body emissive power
G_λ	$W/(m^2 \cdot \mu m)$	spectral irradiation
ρ_λ	-	spectral reflectance
S_{sample}	-	Sample intensity signal, measured by the FTIR heated stage apparatus
S_{BB}	-	Black body intensity signal, measured by the FTIR heated stage apparatus
		F1 model (M_1)
A	1/s	Pre-exponential factor
E_a	J/(mol·K)	Activation energy
R	J/(mol·K)	Universal gas constant
f_γ	-	Austenite volume fraction
		ISV model (M_2)
s	-	Incubation variable
ds/dt	1/s	Instantaneous incubation rate
A,B,C,E	-	Incubation period fitting parameters
dT/dt	K/s	Heating rate
D,F,G,H	-	Transformation period fitting parameters
		Phenomenological Model (M_3)
$\dot{N}$	1/s	Nucleation rate
N	-	Number of nuclei formed
$\dot{T}$	K/s	Heating rate
Q_N	J/mol	Activation energy for nucleation
f_p	-	Pearlite volume fraction
$\dot{v}$	m^3/s	Volumetric growth rate
Q_v	J/mol	Activation energy for growth

$\dot{f}_\gamma$ '	-	Extended austenite volume fraction
$\dot{f}_\gamma$	-	Rate of austenitization
m,m_0	-	Fitting parameters
n, n_0	-	Fitting parameters
A_1,B_1	kJ/mol	Fitting parameters
		Bayesian Model Selection Technique
$p(QoI)$	*	Note, $p(\ldots)$ denotes a probability density function, pdf. For a pdf of Quantity of Interests (QoI), the unit of the pdf is the reciprocal of the unit of QoI. All units for pdfs below are not specified for this reason. '*' denotes that the unit depends on the specific QoI, '-' denotes the variable is unitless.
$\mathbf{b}$ or $\mathbf{b}^{obs}$	-	Data vector of austenite volume fraction
$\mathbf{x}$	*	Vector of model parameter
$p_{po}(\mathbf{x}\|\mathbf{b})$	*	Posterior pdf of $\mathbf{x}$ conditional on the observed data $\mathbf{b}$
$p(\mathbf{b}\|\mathbf{x})$	*	The likelihood pdf
$p_{pr}(\mathbf{x})$	*	Model parameter prior
$p(\mathbf{b})$	*	The evidence
$\mathbf{b}^{mod}(\mathbf{x})$	-	A model prediction of austenite fraction based on parameter $\mathbf{x}$,
$\boldsymbol{\varepsilon}^{meas}$	-	Measurement error
$\boldsymbol{\varepsilon}^{mod}$	-	Model error
$\boldsymbol{\Sigma}^b$	*	Measurement covariance matrix
$\mathbf{L}^b$	*	Cholesky matrix of data vector $\boldsymbol{\Sigma}^b$
$\mathbf{D}$	*	Diagonal matrix of eigenvalues in PCA
$\mathbf{V}$	*	Column vectors eigenvectors corresponding to $\mathbf{D}$
$\mathbf{D}^k$	*	Truncated $\mathbf{D}$, contains k largest eigenvalues, i.e, the covariance of the transformed data, $\mathbf{b}^k$
$\mathbf{V}^k$	*	Truncated $\mathbf{V}$, corresponding eigenvectors of $\mathbf{D}^k$, i.e., the mapping vector that transforms $\mathbf{b}$ to $\mathbf{b}^k$
$\mathbf{b}^k$	-	Data vector $\mathbf{b}$ represented by principal components, i.e., the data vector in PCA data space
$\mathbf{L}^k$	*	Cholesky matrix of $\mathbf{D}^k$

$\mathbf{x}^{pr}$	*	Prior model parameter vector
$\mathbf{\Sigma}^{p}$	*	Prior covariance matrix
$\mathbf{L}^{pr}$	*	Cholesky matrix of $\mathbf{\Sigma}^{p}$
$\mathbf{x}^{MAP}$	*	Maximum a posteriori (MAP) estimate
$\mathbf{L}^{po}$	*	Cholesky matrix of $\mathbf{\Sigma}^{po}$
$\mathbf{\Sigma}^{po}$	*	Posterior covariance matrix
$\mathbf{J}$	*	Jacobian matrix evaluated at $\mathbf{x}^{MAP}$
$\boldsymbol{\mu}$	*	The mean of the pdf describing the model parameter, i.e., $=\mathbf{x}^{MAP}$
σ	*	Standard deviation of the mean, can be found in $\mathbf{\Sigma}^{po}$
$p(x_j\|\mathbf{b})$	*	Marginalized pdf of the j-th parameter in model parameter $\mathbf{x}$
$p(E_a)$	mol·K/kJ	Marginalized pdf of E_a, the activation energy parameter in F1 model
M_i	-	Model i
$P_{po}(M_i\|\mathbf{b})$	*	Model posterior probability of M_i
$p_{po}(\mathbf{x}\|\mathbf{b},M_i)$	*	Posterior pdf of $\mathbf{x}$ conditional on the observed data $\mathbf{b}$, and model M_i
E_i or $p(\mathbf{b}\|M_i)$	*	Evidence conditional on M_i, namely, the model likelihood
$p_{pr}(M_i)$	*	Model Prior
$p_{pr}(\mathbf{x}\|M_i)$	*	Prior pdf of model parameter $\mathbf{x}$ conditional on M_i
B_{ij}	-	Bayes factor between model i and j
C_i	*	Measurement credence for M_i
$F_{b,i}$	*	Relative fit of model i to the data, evaluated at $\mathbf{x}^{MAP}$
$F_{pr,i}$	*	Relative fit of model i to the prior, evaluated at $\mathbf{x}^{MAP}$
ΔC_{ij}	*	Relative measurement credence between model i and j
ΔF_{ij}	*	Relative fit of model i and j

Chapter 1 Introduction

1.1.Research Motivation

Automotive manufacturer often utilizes roller hearth furnace in hot stamping process for producing many structural components, such as the A-/B- pillar of a vehicle. The purpose of furnace heating is to fully austenitize the blank before it can be quenched and formed into fully martensitic components. A common issue in hot stamping is high scrap rate due to incomplete austenitization in the roller hearth furnace, as a result of subpar heating parameters. A complete roller hearth furnace model capable of predicting blank heating and austenitization is needed to help diagnose the production problem. In addition, the roller hearth furnace has to accommodate a variety of steel blanks of different sizes and thickness. This often requires adjustment of the many process parameters, such as the set-point temperatures of many independent heating zones, roller speeds, and blank spacing, etc., to ensure sufficient austenitization while improving energy efficiency. These parameters are often adjusted on a trial-and-error basis, which often lead to suboptimal results and is costly in terms of wasted material and production downtime. A roller hearth furnace model will provide a useful tool for the industrial engineers to arrive at reasonable theoretical process parameters before applying them to the production line. This model based approach can obtain a set of satisfactory parameters much more quickly when the need for adjustment rises. The objective of this work is to establish a complete thermometallurgical model for a roller hearth furnace. In the process, it also pioneers the application of Bayesian model selection as a technique to compare austenitization models.

1.2.Hot Stamping Process

The hot stamping process, also known as Hot Forming Die Quenching (HFDQ), was pioneered in 1977 by Plannja, a Swedish company who used hot stamping to manufacture lawn mower blades. SAAB first adopted hot forming for automotive manufacturing in 1984, specifically to produce components for the Saab 900 [2]. Hot stamped parts are used to decrease vehicle weight without sacrificing crush-worthiness [3], since the stronger martensitic components produced using HFDQ allows for thinner cross-section to be used for the design of many structural components. With

light-weighting, also comes improved fuel efficiency. A 10% weight reduction in the vehicle can improve fuel efficiency by 6-8% [4]. Figure 1 shows a diagram of typical automotive components produced by the HFDQ process. Since its first application, HFDQ has become increasingly popular. In the 2000s, parts made from HFDQ has grown from 107 million parts per year in 2007 [5] to over 450 million parts per year in 2013 [6].

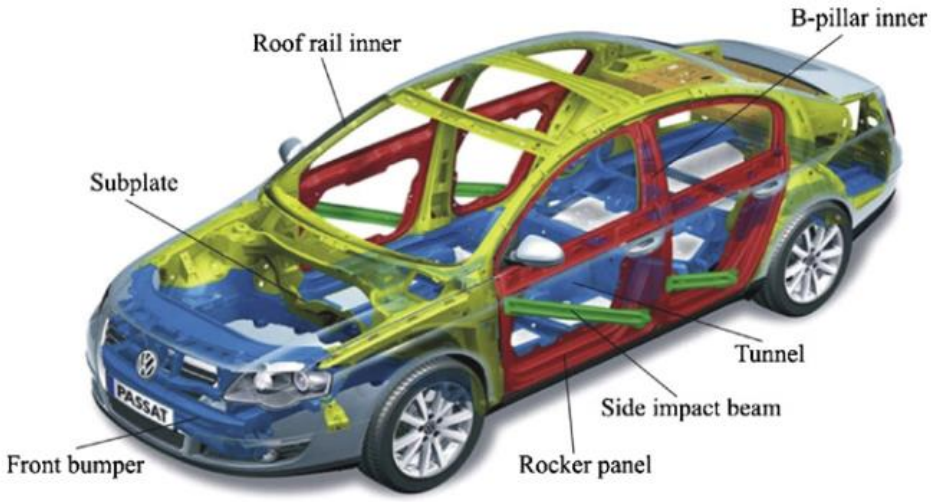

Figure 1: Typical vehicle structural components manufactured using HFDQ [2].

The HFDQ process may either be direct or indirect, as illustrated in Figure 2. The direct hot stamping involves three stages: (1) heating and austenitization of the steel blank in a furnace; (2) blank transfer from the furnace to the die; and (3) die forming and quenching into martensitic components. Indirect hot stamping involves an additional cold pre-forming step prior to furnace heating. The present work focuses on direct hot stamping. The main purpose of furnace heating is to fully transform the blank from its as-received ferrite and pearlite mixture to the more ductile austenite, allowing the forming of intricate geometries while minimizing the forming force required in comparing to cold forming, and reducing the wear on tooling [7, 8]. The most commonly used material for HFDQ are manganese boron steels, such as 22MnB5 [2], which is often coated with a Al-Si layer that protects the steel from oxidation and decarburization while heating [9]. This coating melts at around 575 °C [10], and then resolidifies and transforms into Al-Si-Fe intermetallic layer to provide long term corrosion resistance [11, 12]. The secondary purpose of the furnace heating is to facilitate the coating transformation reaction.

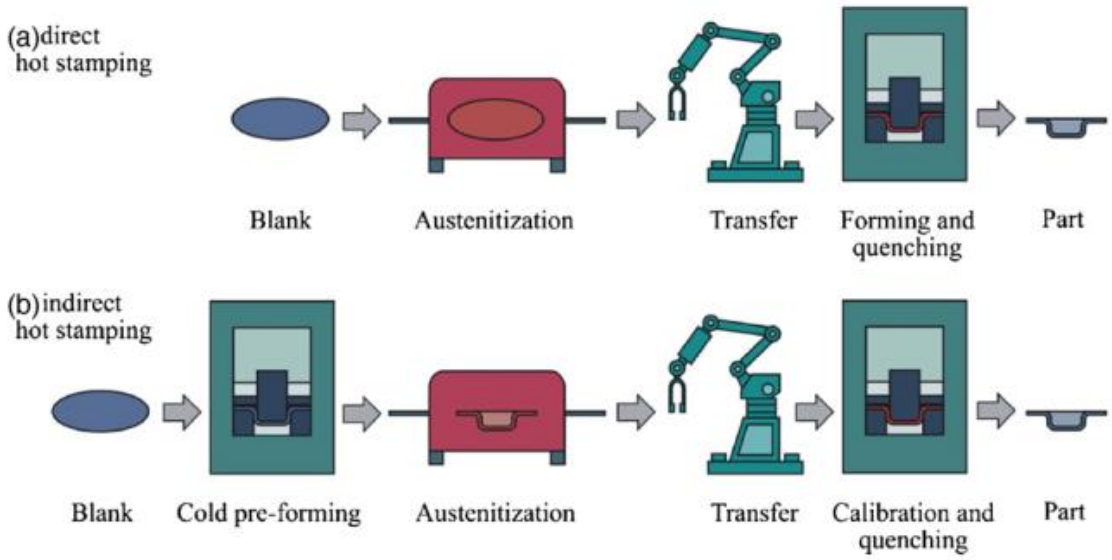

Figure 2: Schematic of (a) direct hot stamping and (b) indirect hot stamping [2].

Traditionally, the furnace used for heating is a roller hearth furnace [13], such as the one shown in Figure 3. Other heating methods such as batch furnaces [14], direct contact heating [15, 16, 17], and induction heating [18] are being explored but not yet widely adopted for HFDQ process.

Figure 3: Roller hearth furnace at Formet Industries [19].

A typical roller hearth furnace can range from 30 to 40 meters long [2], and comprises many independently controlled heating zones, each heated with natural gas fired radiant tube burners. These burners can be located both above and below the ceramic rollers that convey the blanks

through the furnace and are activated via a hysteresis control system. Each heating zone has a control thermocouple (TC), if the control TC measures below the set-point of this zone, the burners are turned on, if the TC measures above the set-point, the burners are turned off. Figure 4 shows a schematic of a roller hearth furnace.

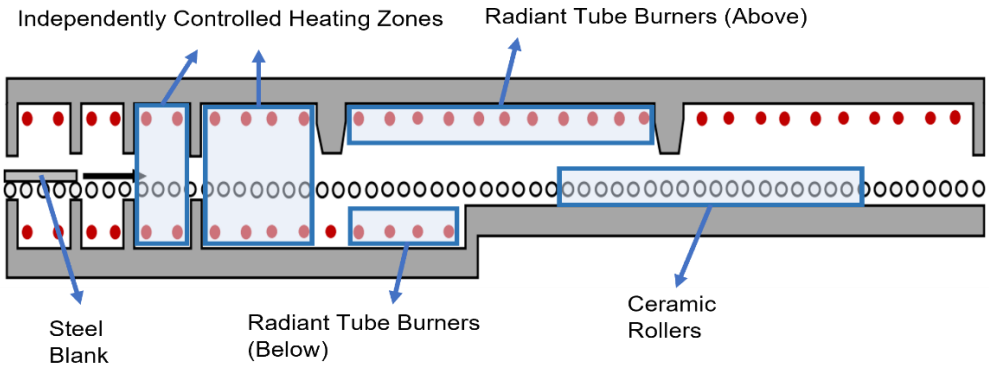

Figure 4: Schematic of a roller hearth furnace cross section [20]

The furnace parameters, consisting of zone set-point temperatures, roller speed, and other ancillary parameters, must be adjusted to ensure full austenite transformation and proper coating transformation while minimizing cycle time. These process parameters are different depending on the blank shapes and thickness, and they are often chosen through trial-and-error, which rarely results in optimal values, cost precious production time and waste in materials. Accordingly, there exists a need for an accurate roller hearth furnace model capable of predicting both the heating and austenitization process, which is part of the focus of this work.

1.3.Literature Review on Furnace Models and Austenitization Models

Since furnace heating tends to be very energy intensive, challenging to control, and has crucial impact on mechanical properties of the material, its modelling and optimization has long been a popular topic in the industry. The modelling of different industrial furnaces, such as re-heating furnaces for steel slabs [21-25], and roller hearth furnace for steel blanks [26-29] has been well documented. Some of the studies employ a detailed simulation based approach, such as computational fluid dynamics (CFD) [29], or finite volume method (FVM) [24]. Others adopt a more simplified mathematical model with varying level of details, such as combustion for the heaters [26, 27], the involvement of non-participating gaseous media [25].

Most of the modelling work mentioned above focus solely on the temperature prediction, without considering the effect of phase transformation of the steel. This omission can affect the prediction accuracy, as shown by the work of Ganesh et al. [30], who built upon the work by Heng et al. [26] by incorporating the latent heat of austenitization and arrived at different optimal results. For the purpose of roller hearth furnaces used for HFDQ, austenitization is critical to ensure component quality downstream. Hence, having a furnace model that considers both heating and austenitization can be a useful tool for industrial engineers who design the process.

Taking the approach of [31, 32, 33], Twynstra et al. [34] indirectly incorporated the effect of austenitization by augmenting the specific heat of 22MnB5 steel, c_p, with the latent heat of austenitization, to form the effective specific heat, $c_{p,eff}$. The latent heat of austenitization (assumed to be 85 kJ/kg [35]) was uniformly distributed between T_{Ac1} and T_{Ac3}. Jhajj et al. [36] built upon this idea, and derived $c_{p,eff}$ from inverse analysis of calorimetric data obtained from 22MnB5 furnace trials.

Improving on the model by Jhajj et al. [19, 36], Verma et al. [20, 37] developed a roller hearth furnace model framework for 22MnB5 steel, which couples a heat transfer submodel with an austenitization submodel. This approach explicitly considers the phase transformation kinetics, and not only improves temperature prediction accuracy comparing to the above mentioned models, but also provides a better understanding of the phase transformation process within the roller hearth furnace. This, in turn, requires an austenitization kinetics model.

Many candidate models have been proposed to capture the transformation process, each with varying degrees of complexity. Di Ciano et al. [38] developed a simple first-order (F1) austenitization model, which was used by Verma et al. [20] in his work. The F1 model is mathematically equivalent to a Johnson-Mehl-Avrami-Kohnogorov (JMAK) type model with n = 1. Di Ciano et al. derived two sets of model parameters for 22MnB5 steel, based on low (1-5 °C/s) and high (10-20 °C/s) heating rate dilatometry data collected in a Gleeble thermo-mechanical simulator. Verma et al. [20] also used a more detailed phenomenological model by Li et al. [39] applicable to both full and partial austentization (or intercritical annealing). This semi-physical model considers the effect of nucleation, growth and impingement and has 10 model parameters. Luo et al. [40] introduced the Isoconversional Method (IM) model for predicting austenitization of SA508 Gr.3 steel. The IM model is also based on the JMAK equation but it allows model

parameters to vary throughout the phase transformation process. Zhao et al. [41] adapted this approach to model austenitization of 22MnB5 steel and integrated it into the roller hearth furnace model framework. Huang et al. [42] proposed an Internal State Variable (ISV) model for the austenitization of 60Si2CrA steel, a semiempirical model that consists of incubation and transformation periods accounting for the effects of temperature, heating rate, and volume fraction of austenite.

1.4. Bayesian Model Selection Technique

With the many available candidate austenitization models, comes the challenge of deriving their model parameters and assessing their relative performance. Conventionally, the parameters of these austenitization models are often derived from nonlinear regression to dilatometry data, and the models themselves are assessed based on their relative goodness-of-fits to this data. Unfortunately, this process does not address measurement uncertainty in the dilatometry data, nor does it account for model complexity. Increasingly complex models are generally expected to provide a superior goodness-of-fit, but this does not necessarily translate into a more accurate or "physical" model. As the number of model degrees-of-freedom increases, the model fitting process becomes progressively ill-posed and unavoidable measurement errors and artifacts begin to have an outsized effect on the inferred quantities. Consequently, over-turned models will accurately describe calibration data but may produce erroneous results when the model is applied in a different setting, for instance to austenitization within a furnace or during model-based optimization. These shortcomings call for a more statically rigorous approach to model evaluation.

In Bayesian model selection [43], models are quantitatively ranked based on their fit to the data, but also on the number of model parameters, the amount of prior knowledge available about these parameters, the goodness-of-fit between the inferred quantities-of-interest (QoI) and the prior knowledge about the values the QoI are likely to hold. Examples include applications in the social sciences [44], fluid mechanics [45], astronomy [46], and laser-based diagnostics [47]. This could serve as a better way to derive model parameters and evaluate the trade-off between model complexity and accuracies.

1.5. Thesis Outline

This thesis is divided into seven chapters: the background on HFDQ and roller hearth furnace is introduced, along with literature review on furnace models and austenitization models; the material properties of USIBOR® 1500 is listed; the roller hearth furnace model, including the heat transfer submodels and candidate austenitization submodels are discussed; experimental methods used in the study are explained; Bayesian model selection is introduced and used to select an optimal austentization submodel; validations are done on both austenitization model and the overall furnace model; finally, the conclusion of this work and future improvements are laid out.

Chapter 2 discusses the details of USIBOR® 1500, including its mechanical properties, the austenitization mechanism, as well as the Al-Si coating. The coating evolves during the heating process and affects the radiative properties of the blank.

Chapter 3 introduces the roller hearth furnace model, which couples a heat transfer submodel and an austenitization submodel. The heat transfer model considers convection and radiation heat transfer. Extensive effort is put on the quantification of evolving radiative properties. Three candidate austenitization submodels are also introduced.

Chapter 4 details the experimental methods used. Dilatometry data is used to derive and compare austenitization models; quantitative metallography is used to valid the dilatometry data; and roller hearth furnace trials are gathered using instrumented blanks.

Chapter 5 establishes the procedures for applying Bayesian model selection technique on candidate austenitization models. The theoretical groundwork is laid down and necessary steps taken to mitigate some numerical issues are also discussed. An optimal model is quantitively chosen by weighing the relative accuracy and complexity of all candidate models.

Chapter 6 first visually compares the three austenitization candidate models with the dilatometry data used in the derivation process, as well as additional dilatometry data collected on a similar set-up. This further illustrates the result of Chapter 5 and shows how the optimal model performs. The overall furnace model is then validated by two furnace trials.

Chapter 7 summarizes the main conclusions and discusses the potential application and refinements of the model.

Chapter 2 Material Properties and Heat Treatment

2.1. Usibor® 1500

The most commonly used HFDQ material and the focus of this work is Al-Si coated 22MnB5 steel. This steel is produced by ArcelorMittal under the tradename Usibor® 1500. The Al-Si coating melts at around 575 ℃ and transforms into an Al-Si-Fe intermetallic layer to provide long term corrosion resistance [10]. The coating transformation has drastic impact on the surface roughness, which in turn affects the radiative properties of the material. Since the dominant mode of heat transfer inside a roller hearth furnace is radiation heat transfer, the change in radiative properties greatly influences the heating process. Sec. 2.3 and 3.2.3 discuss these in greater details. The 22MnB5 steel, and many other steel alloys such as 20MnB5, 8MnCrB3, are commonly used for HFDQ process because they can be heated and quenched into fully martensitic components [48] under more achievable cooling rates. This high formability comes from the addition of alloying elements such as B, Mn, and Cr, which shifts the bainite formation nose in the time temperature transformation (TTT) curve more to the right, allowing a lower quench rate to achieve fully martensitic components. Figure 5 (b) shows a hypothetical TTT curve that illustrates this effect. A typical composition of the 22MnB5 steel examined using optical emission spectrometry (OES) is listed in Table 1:

Table 1. Composition of 22MnB5 steel used in dilatometry measurement [49].

Elem	C	Mn	P	S	Si	Ni	Cr	V	Ti	Al	B	Ca
%	0.23	1.14	0.01	0.003	0.23	0.01	0.23	0.005	0.035	0.05	0.002	0.002

To achieve full martensitic transformation, the material needs to be first fully austenitized, usually using a roller hearth furnace. Figure 5(a) shows a Fe-C phase diagram of 22MnB5 steel. The as-received microstructure of Usibor® 1500 is approximately 80% ferrite and 20% pearlite [38]. Austenitization starts at the onset critical temperature, T_{Ac1}, reported in literature to be approximately 730 ℃, and finishes at T_{Ac3} which is approximate 880 ℃ [38, 50, 51]..

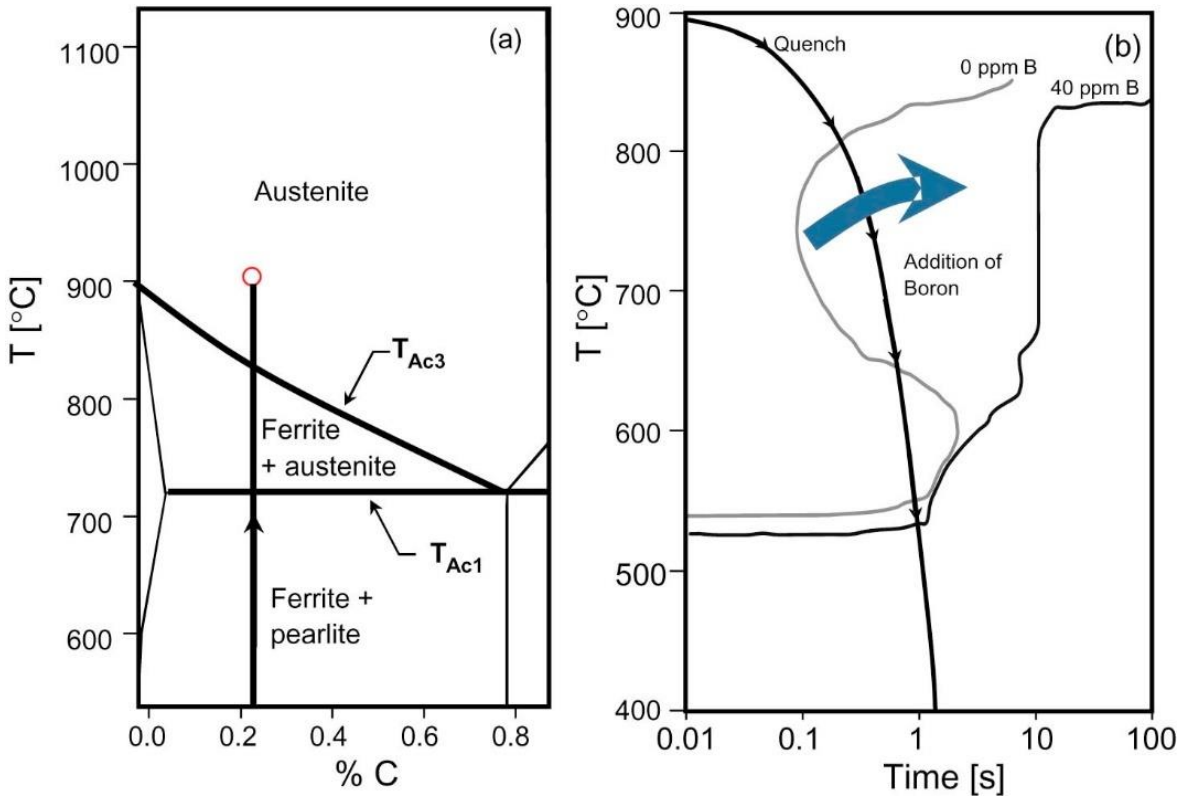

Figure 5: (a) Fe-C phase diagram, illustrating the austenitization process of 22MnB5 steel; (b) hypothetical time temperature transformation (TTT) curve showing the addition of boron causes the shift of bainite nose, lowering the quench rate requirement for full martensitic transformation [52] (only a schematic for illustration, not to scale).

Figure 6 illustrates the continuous cooling curve (CCT) diagram of 22MnB5 steel derived by Naderi [48]. With the minimum required cooling rate of 25 ℃/s, martensite formation starts at *M*s = 410 ℃ and finishes at M_f = 280 ℃ [2, 39, 53]. This information along with some other critical mechanical properties for 22MnB5 steel is summarized in Table 2.

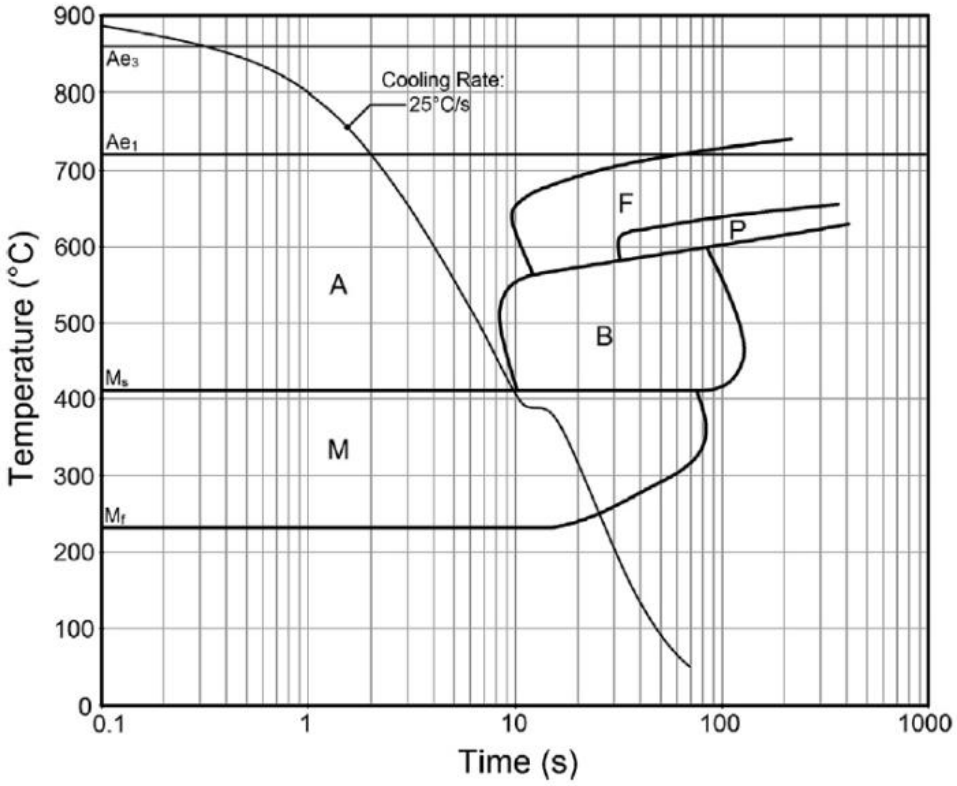

Figure 6: Continuous cooling transformation (CCT) curve for 22MnB5 steel [48], A, F, P, and M denotes austenite, ferrite, pearlite, and martensite respectively.

Table 2: Summary of mechanical properties of 22MnB5 steel [2]

T_{Ac1} [°C]	730	
T_{Ac3} [°C]	880	
M_s [°C]	410	
M_f [°C]	280	
Critical cooling rate [°C/s]	25	
Yield Strength [MPa]	As-Received	457
	Hot Stamped	1010
Tensile Strength [MPa]	As-Received	608
	Hot Stamped	1478

2.2. Austenitization Kinetics in Roller Hearth Furnaces

Over the past decades, austenitization in ultra-high strength steel (UHSS) has been extensively studied due to the increasing popularity of hot stamping. The understanding of austenitization will result in better control of the mechanical properties and more efficient process. Asadabad et al. [54] studied the effects of temperature and soaking time on austenitization in dual phase steels; Oliveira et al. [55] investigated the influence of heating rate on critical austenitization formation temperatures (T_{Ac1}) in low carbon steel. Cai [56] studied full austenitization process under continuous heating, while Li et al. [53] characterized the effects of heating rate and temperature on austenitization of boron steels under both isothermal and non-isothermal conditions.

22MnB5 is an hypoeutectoid steel (carbon content less than 0.77 wt% [57]), with an initial microstructure of proeutectoid ferrite and pearlite. Pearlite is a lamella structure of eutectoid ferrite (α) and cementite (θ). Sketch No.1 in Figure 7 (a) shows a schematic of the as received microstructure. Under equilibrium condition, the eutectoid reaction starts at T_{Ae1}, as shown in Figure 7(b), and the transformation completes at T_{Ae3}. T_{Ae1} is approximately 723 ℃ and T_{Ae3} is defined in relation to the transformation completion time of pure iron, at 910 ℃. T_{Ae3} decreases with the addition of carbon content since the solubility of carbon in ferrite (α) is low, and ferrite to austenite (α → γ) transformation can only happen at higher temperatures. The austenitization process is primarily a carbon diffusion-controlled process (with some Fe self-diffusion) under most industrial heating rates and temperatures. Since the diffusivity of carbon in steel is 10^5-10^6 greater than that of substitutional solutes such as Mn [58]. Only at lower temperatures that the process switches to manganese diffusion-controlled [59].

Austentization is a nucleation and growth process [60, 61] that can be divided into two main stages. The process begins with rapid pearlite dissolution, where austenite nucleation mainly happens at the ferrite-cementite interface inside the pearlite colonies, or at the interfaces between different pearlite colonies [62, 63]. The newly formed austenite grows and replaces the eutectoid ferrite while cementite dissolves in the austenite (γ). This process happens quickly due to the short diffusion distances between adjacent cementite lamellae [59, 64]. This stage is denoted by "1→2" in Figure 7. Once all pearlite colonies have transformed to austenite, the remaining proeutectoid ferrites transforms as the carbon diffuses from the carbon-rich austenite grain to the ferrite-

austenite grain boundaries, expanding the boundaries toward ferrite regions until the transformation is complete [59, 63, 65]. During this process, no further nucleation occurs, only the growth of existing austenite regions at the expense of remaining ferrite regions [59, 66]. This stage is shown in Figure 7 as process 2→3. Note that full austentization is only possible if T_{Ae3} is reached. If isothermal soaking occurs between T_{Ae1} and T_{Ae3}, only partial austenitization is possible [54, 67], and the amount depends on the soaking temperature [53] (hence the region between T_{Ae1} and T_{Ae3} is called intercritical region). However, under most practical HFDQ industrial application, the heating process is continuous. The equilibrium onset (T_{Ae1}) and complete (T_{Ae3}) temperatures shifts to higher values (T_{Ac1} and T_{Ac3} as shown in Figure 7) [68]. The determination of T_{Ac1} and T_{Ac3} depends on the heating rate [55]. Di Ciano et al. [38] experimentally determined that for 22MnB5 at lower heating rates (1-5 ℃/s), T_{Ac1} and T_{Ac3} are between 723-740 ℃ and 850-855 ℃ respectively. This is generally confirmed by other empirical correlations and experimental work available in the literatures [54, 64].

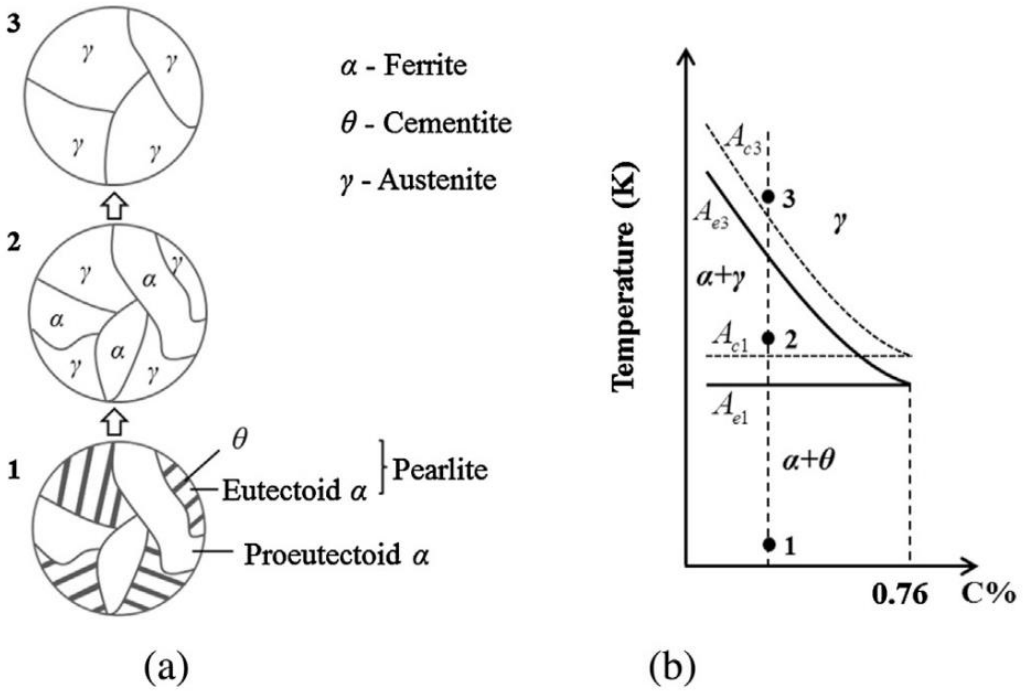

Figure 7: Austenitization schematics of a hypoeutectoid steel illustrating (a) different microstructures; (b) their corresponding places in a Fe-C phase diagram [53].

2.3. Al-Si coating

The steel blank used for HFDQ is often covered with an Al-Si coating that protects the steel from oxidation and decarburization while heating [9]. Usibor® 1500 comes with two common coating weights AS80 and AS150, having a nominal coating thickness of 15 μm and 25 μm respectively, and a nominal coating composition of 90%-Al and 10%-Si in wt% [69] (The only coating weight currently used in present study is AS150). This coating melts at around 575 °C [10], resolidifies and transforms into Al-Si-Fe intermetallic layer to provide long term corrosion resistance [11, 12]. Figure 8 shows scanning electron microscope (SEM) images of as-received AS80 and AS150 coating conditions. Distinct ternary intermetallic compounds such as τ_5 (Al_7Fe_2Si or $Al_{7.4}Fe_2Si$) and τ_6 ($Al_{4.5}FeSi$) and some iron oxides (Fe-O) can be identified.

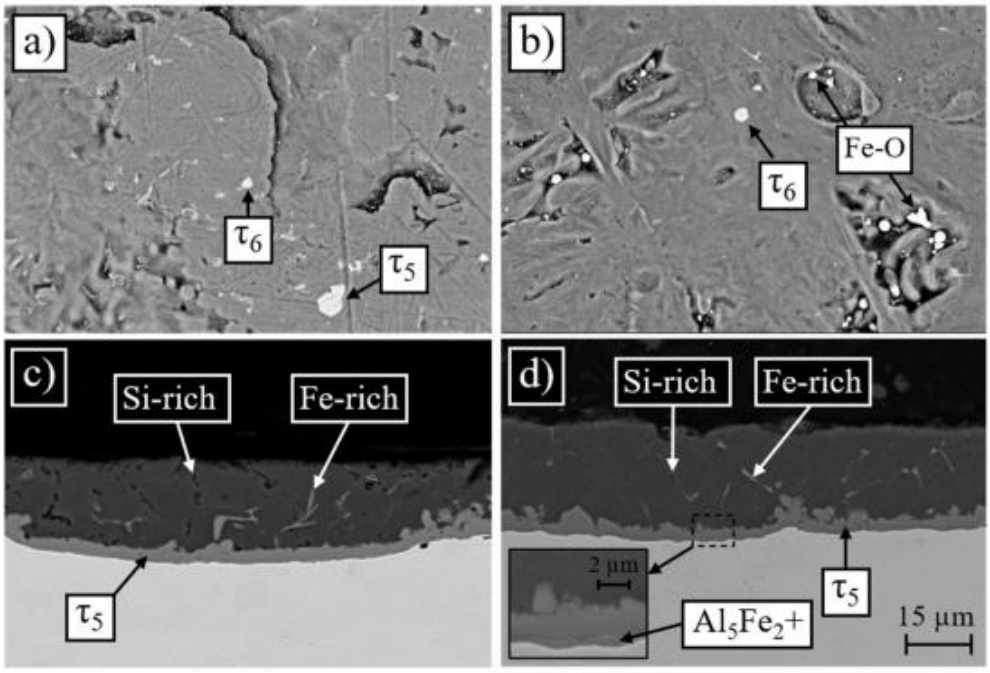

Figure 8: As-Received SEM top view image of (a) AS80 and (b) AS150, and cross-sectional view of (c) AS80 and (d) AS150 [70].

As the coating melts, iron diffuses from the steel substrate to the surface and reacts with the coating, manifesting as intermetallic layers such as τ_5 progressing to the top surface [71, 72]. As expected for a diffusion process, higher heating temperature allows iron to diffuse faster and

facilitates the coating phase transformation [73]. Upon further heating, the coating resolidifies and grows thicker, forming a multi-layer microstructure as the coating transformation completes at around 930 ℃. Klassen et al. [70] conducted a thorough literature review and found some discrepancy in the characterization of the final coating compositions. Researchers reported different combinations and distributions of various intermetallic compounds including, $Al_2Fe_2Si_3$, Al_5Fe_2, AlFe, Al_2Fe_2Si, Al_2Fe [71, 74-76]. This indicates that the coating evolution is sensitive to the heating parameters. For the purpose of HFDQ, the coating thickness should be kept under 40 μm for proper weldability [77] and the diffusion layer should be kept under 20 μm for coating durability [78]. The coating evolution also impacts the heating process, as the surface morphology changes will result in roughness change, which in turn, affects radiative properties such as emissivity and absorptivity. Barreau et al. [79] reviewed and summarized the series of melting reaction occurring during the coating evolution,

$$\begin{cases} 577°C: Al + Si + \tau_6 \rightarrow L \\ 615°C: Al + \tau_6 \rightarrow \tau_5 + L \\ 620°C: \tau_5 + Al \rightarrow L + FeAl_3 \\ 655°C: FeAl_3 + Al \rightarrow L \\ 855°C: \tau_5 \rightarrow FeAl_3Si + FeAl_3 + L \end{cases} . \quad (2\text{-}1)$$

The coating partially melts during the first reaction, while the second and third reaction creates a smooth reflective surface. Klassen et al. [10, 70] developed an in-situ method to infer the surface roughness change as the blank is being heated in a furnace. Figure 9 shows an inferred surface roughness evolution as samples are being heated in a 900 ℃ muffle furnace. It can be observed that both AS80 and AS150 coating becomes smoother as the coating melts, and rougher as the coating transforms and resolidifies. The impact of this change on the radiative properties are discussed in Sec.3.2.3.

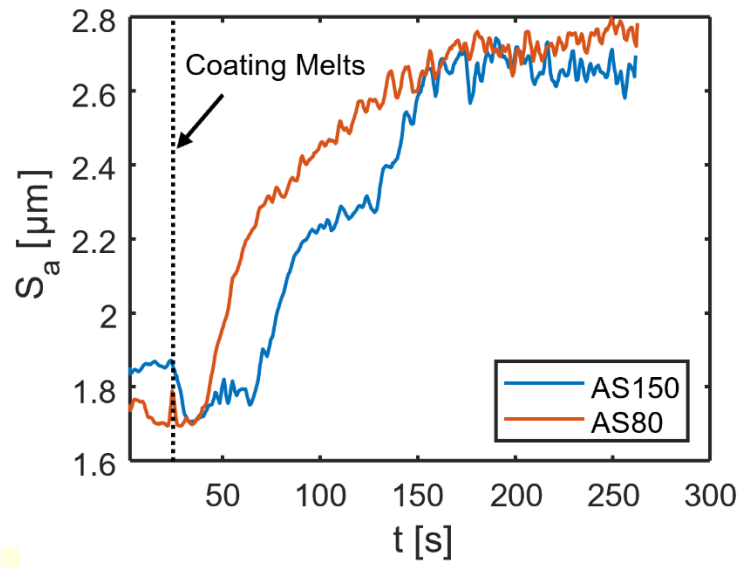

Figure 9: Inferred surface roughness of AS80 and AS150 coating weight, in a muffle furnace set at 900 ℃ [70].

The liquid phase of the Al-Si coating also causes some concerns. Firstly, the liquified coating can cause the blank to slide on the rollers, which affects the designed blank spacing and complicates the automation process of furnace-to-press transfer; Secondly, the liquid coating can penetrate into or build up on the ceramic rollers, resulting in costly damage [80]. Figure 10 shows an example of a damaged roller. Process designers have most resorted to heuristically adjusting the roller speeds and zone set-points to mitigate this issue.

Figure 10: An image showing ceramic rollers heavily damaged by Al-Si coating deposits

Chapter 3 Furnace Model

3.1.Roller Hearth Furnace Model Framework

Verma et al. [20] proposed a model framework for predicting both the heating of the blank as well as the austenite transformation by coupling a heat transfer submodel with an austenitization submodel. Figure 11 shows a flowchart illustrating the components of such model framework.

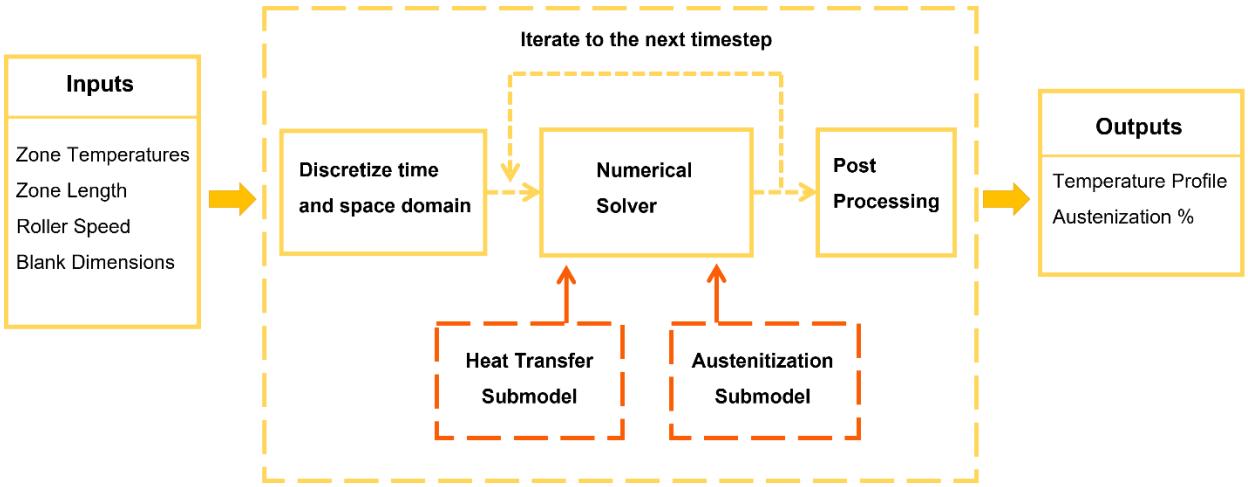

Figure 11: Flowchart illustrating the framework of the roller hearth furnace model

The model takes key furnace and material parameters as inputs and outputs the temperature profile and austenite phase fraction as a function of time. The heat transfer submodel evaluates the change in temperature of the blank based on convective and radiative heating, while the austenitization submodel predicts the phase transformation once the blank reaches onset austenitization temperature, T_{Ac1}. The two submodels are coupled together through the latent heat of austenitization. The details of each submodel are introduced in Sec. 3.2 and 3.3.

3.2.Heat Transfer Submodel

There are several key assumptions made to simplify the heat transfer modelling for a more practical industrial deployment of the model. Each heating zone of the furnace is assumed to be relatively large and isothermal comparing to the blank. Since the furnace typically operates at high temperatures (typically 750 to 950 °C), the dominant mode of heat transfer is radiation heat

transfer, although convection heat transfer by the hot furnace air is also considered. The contact areas between the blank and the round rollers are assumed to be infinitesimally small, therefore conduction between the blank and the ceramic rollers is neglected. Figure 12 shows the control volume of a blank which has uniform temperature, same as its surface temperature, T_s (due to the relatively small thickness of a typical blank, the blank is assumed to be uniform in temperature throughout its thickness, therefore $T_{blank} = T_s$). The ambient temperature, T_{amb}, for convection and surrounding temperature, T_{surr}, for radiation are both assumed to be equal to the furnace set-point of the current zone. This is the ideal case, where each zone is physically separated by baffles that provide a thermal barrier. However, roller hearth furnaces can be configured not to have physical baffles for every zone, such as the case for the furnace trials discussed in Sec. 6.2. In that case, unbaffled neighboring zones with different set-points can affect each other thermally, and it becomes difficult to maintain their own set-points under the influence of other zones.

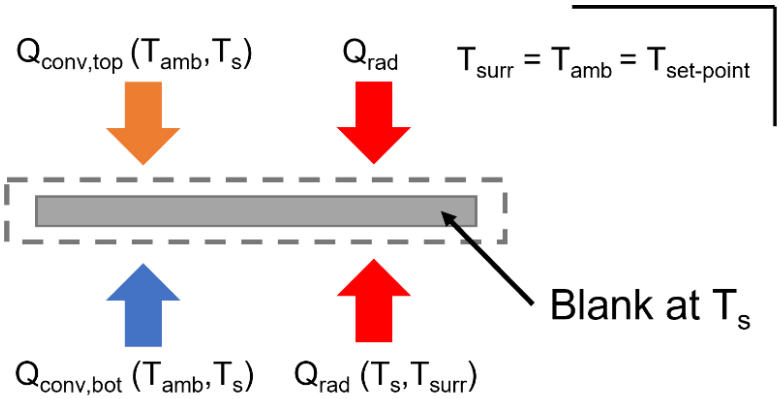

Figure 12: Diagram illustrating the assumption made for heat transfer model

The overall governing equation of the heat transfer submodel is described in Eq. (3-1),

$$\rho c_p V \frac{dT}{dt} = Q_{rad} + Q_{conv} - \rho V \Delta h_\gamma \frac{df_\gamma}{dt}, \tag{3-1}$$

where ρ and c_p denotes the density of the blank and specific heat, respectively [14], Δh_γ is the latent heat of austenitization (assumed to be 85 kJ/kg [20, 35]), df_γ/dt is the instantaneous austenitization rate, Q_{conv} and Q_{rad} are the energy received from convection and radiation heat transfer. The austenitization submodel predicts the austenitization rate which is discussed in detail in Sec. 3.3. Equations governing convection and radiation heat transfer are presented in Sec. 3.2.1 and 3.2.2

respectively. The temperature dependent properties such as density, specific heat and conductivities for Usibor® 1500 are provided by the ArcelorMittal and are attached in Appendix A. These properties will be linearly interpolated based on the blank temperature.

3.2.1. Convection Heat Transfer

Due to the relatively slow travel speed of the blank (less than 1 m/s [20]), the air within the furnace is assumed to be quiescent, therefore the convection mode is natural convection. The rate of heat transfer between the blank and ambient air is governed by Newton's law of cooling,

$$Q_{conv} = Q_{conv,top} + Q_{conv,bot} = A\left[\bar{h}_{top}\left(T_{amb} - T_s\right) + \bar{h}_{bot}\left(T_{amb} - T_s\right)\right], \tag{3-2}$$

where T_{amb} is the ambient temperature, which is assumed to be the same as the set-point temperature of the current zone, T_{s} is the blank surface temperature (blank temperature is assumed to be spatially uniform), A is the single-side area of the blank, $\bar{h}_{\text{top}}$ and $\bar{h}_{\text{bot}}$ are the average natural convection coefficient for the top and bottom surface respectively. These are determined based on Nusselt number,

$$\overline{Nu} = \frac{\bar{h}L_c}{k_{air}}, \tag{3-3}$$

where L_{c} is the characteristic length of the blank, defined as $L_{\text{c}} = A/P$ (A is the surface area of the blank and P is the perimeter), k_{air} is the temperature dependent thermal conductivity of air, determined at film temperature, T_{film},

$$T_{film} = \frac{T_{amb} + T_s}{2}, \tag{3-4}$$

The correlation for the Nusselt numbers can be found from [81] to be,

$$\overline{Nu}_{top} = 0.52 Ra_L^{\,0.2}, \tag{3-5}$$

$$\overline{Nu}_{bot} = 0.54 Ra_L^{\,0.25}, \tag{3-6}$$

where Ra is the Rayleigh number defined by,

$$Ra_L = \frac{g\beta\left(T_{amb} - T_s\right)L_c^{\,3}}{\nu_{air}\alpha_{air}}, \tag{3-7}$$

where ν_{air} and α_{air} are the thermal diffusivity and kinematic viscosity of air, taken at T_{film}, β is the volumetric thermal expansion coefficient for air, $\beta = 1/T_{film}$. The properties of air (k_{air}, ν_{air}, and α_{ai}) are available in the heat transfer textbook by Bergman, et al. [81].

3.2.2. Radiation Heat Transfer

The furnace environment is assumed to be isothermal and relatively large comparing to the blank dimensions, i.e., the small object in large isothermal enclosure assumption. This assumption has two implications: firstly, the irradiation from the furnace environment to the blank can be approximated as black body irradiation at the surrounding temperature; Secondly, the blank has negligible impact on the furnace environment itself. With this assumption, the radiation heat transfer can be greatly simplified. The net rate of radiation heat transfer is then,

$$Q_{rad} = 2A\sigma\left[\alpha\left(T_s, T_{surr}\right)T_{surr}^{\,4} - \varepsilon\left(T_s\right)T_{surr}^{\,4}\right], \tag{3-8}$$

where T_{surr} is the surrounding temperature, assumed to be the zone set-point, $\sigma = 5.67 \times 10^{-8}$ W/(m^2·K^4) is the Stefan-Boltzmann constant, A is the single-side surface area of the blank ($2A$ since we assume both side of the blank are irradiated equally by the furnace environment) and α and ε are the total absorptivity and emissivity.

3.2.3.Radiative Properties

Since the dominant form of heat transfer in a roller hearth furnace is radiation, the radiative properties, α and ε, in Eq. (3-8) have crucial impact on the accuracy of the model. However, the quantification of these properties is further complicated by the evolving nature of the surface morphology as discussed in Sec. 2.3. ArcelorMittal [82] provided some spectral emissivity (ε_λ) data at various temperature shown in Figure 13. After the melting of the coating at 575 ℃, the spectral emissivity decreases significantly (600 ℃ curve in Figure 13) compared to the as-received state. As the coating solidifies and as iron diffuses to the surface to form rougher intermetallic layers, the spectral emissivity increases gradually until it is fully transformed.

The total emissivity at a given blank temperature, T_{blank}, can be found using [81],

$$\varepsilon = \frac{\int_0^\infty \varepsilon_\lambda \left(T_{blank}\right) E_{\lambda,b}\left(T_{blank}\right) d\lambda}{E_b\left(T_{blank}\right)} = \frac{\int_0^\infty \varepsilon_\lambda \left(T_{blank}\right) E_{\lambda,b}\left(T_{blank}\right) d\lambda}{\sigma {T_{blank}}^4}, \tag{3-9}$$

where $E_{\lambda b}$ is the spectral blackbody emissive power defined by Planck's distribution, and E_b is the total blackbody emissive power. Based on the spectral emissivity data provided by the manufacturer, the total emissivity at different blank temperature is calculated and shown in Figure 14. The values between data points are linearly interpolated since no sudden change in radiative property is expected after the initial melting of the coating.

The total absorptivity depends on the spectral irradiation from the furnace environment, G_λ, as well as the spectral absorptivity of the blank, α_λ. It can be calculated using [81],

$$\alpha = \frac{\int_0^\infty \alpha_\lambda \left(T_{blank}\right) G_\lambda \left(T_{surr}\right) d\lambda}{\int_0^\infty G_\lambda \left(T_{surr}\right) d\lambda}, \tag{3-10}$$

With the assumption that the blank surface is diffuse, the Kirchoff's law states that spectral emissivity equals to spectral absorptivity, i.e., $\varepsilon_\lambda = \alpha_\lambda$. Since the furnace environment is assumed to be relatively large and isothermal comparing to the blank, its irradiation can be approximated as black body irradiation at the surrounding temperature, i.e., $G_\lambda = E_{\lambda b}$. Hence, Eq. (3-10) becomes

$$\alpha = \frac{\int_0^\infty \varepsilon_\lambda \left(T_{blank}\right) E_{\lambda,b}\left(T_{surr}\right) d\lambda}{E_b\left(T_{surr}\right)} = \frac{\int_0^\infty \varepsilon_\lambda \left(T_{blank}\right) E_{\lambda,b}\left(T_{surr}\right) d\lambda}{\sigma {T_{surr}}^4}, \tag{3-11}$$

The total absorptivity derived using Eq. (3-11) based on the manufacturer provided data is shown in Figure 14. This curve is calculated assuming a furnace environment of 900 °C, which is approximately the case for most roller hearth furnaces

Although the manufacturer provided data offers a good starting point, it is unclear how exactly this data is obtained in terms of experimental set-up and heating schedule. Since the coating transformation is affected by not only temperature, but also heating rate [79], there is scepticism as to how applicable this data is to a roller hearth furnace heating environment. Jhajj et al. [36] and Shi et al. [83] did extensive work to study the coating transformation and its effect on the radiative

properties. Through their experiment, they discovered that the radiative properties below the melting point of the coating is consistent with the manufacturer provided result, but the result differs beyond that point, depending on the heating rate and coating morphology. Jhajj et al. [36] carried out in-situ spectral emissivity measurements using an NIR spectrometer fitted to a Gleeble 3500 thermomechanical simulator. The advantage of using such a set-up is that the Gleeble is capable of simulating the heating process based on a typical roller hearth furnace blank heating profile. Therefore, the result is more applicable to be used in the roller hearth furnace model. The NIR spectrometer has a measurement range of 0.9 - 2.5 μm; therefore, the in-situ NIR spectral emissivity is supplemented by ex-situ FTIR reflectance measurements (ρ_λ) of samples heated and quenched at various temperatures (700, 800, 900, and 935 ℃) which has a range of 2.5 - 25 μm. The spectral emissivity, ε_λ, can be obtained from spectral reflectance, ρ_λ to be,

$$\varepsilon_\lambda = 1 - \rho_\lambda. \tag{3-12}$$

Although it is not ideal to use ex-situ measurements, considering that total emissivity and absorptivity in Eq. (3-9) and (3-11) are essentially weighted average of the spectral values based on the Planck distribution, $E_{\lambda b}$, which heavily favors the shorter wavelength at higher temperature, it is more important to accurately capture the shorter wavelength. Jhajj [19] also noted that air-quenching results in distortions of the coating surface between 575-700 ℃ due to airflow over the molten coating layer, therefore, the FTIR measurement on quenched samples cannot be used for this temperature range. Instead, the in-situ NIR values was extended into the mid-infrared range (2.5-25 μm). The total emissivity and absorptivity derived by Jhajj et al. [36] is compared with the manufacture provided values in Figure 14. It can be observed that the two sets of results agree in general trend, both drop off after coating liquification, and slowly climbs back up. The result by Jhajj et al. is generally higher during the coating resolidification process (600 - 800 ℃).

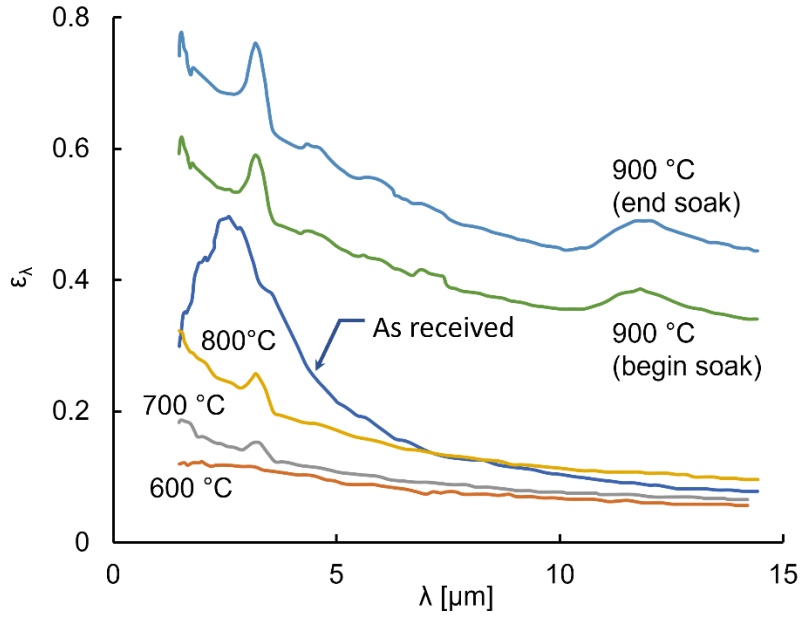

Figure 13: Spectral emissivity provided by the manufacturer [82]

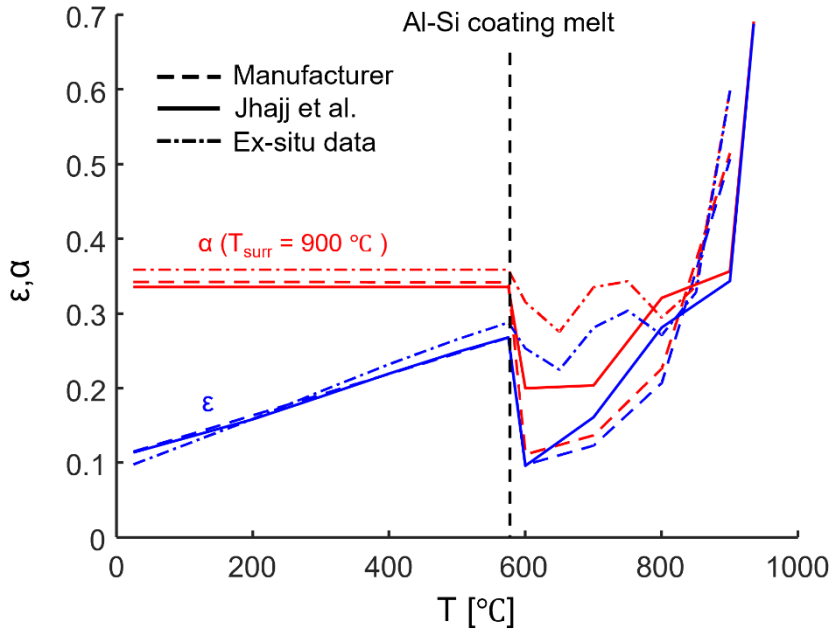

Figure 14: Total emissivity and absorptivity based on manufacturer provided spectral emissivity and values obtained experimentally by Jhajj et al. [36]

Additional ex-situ FTIR measurements are also carried out using samples heated in a 900 ℃ muffle furnace. The samples were extracted and quenched at various temperatures. With a combination of different types of detectors, the ex-situ FTIR measurements cover from 0.5 to 25 μm. The derived total emissivity and absorptivity is also shown in Figure 14 for comparison. Note that the ex-situ result confirms the general trend of the radiative properties change but is considerably higher during the resolidification phase (600 - 800 ℃). This is to be expected, since the ex-situ nature negates the liquid phase of the coating, therefore the ex-situ data cannot capture the drop in emissivity due to the highly reflective molten surface. Klassen, et al. [10] also believed that the quenching process used to obtain the sample could disrupt the surface, based on comparison of in-situ and ex-situ laser reflectance measurements.

3.2.3. FTIR In-situ Heated Stage Apparatus

Attempts were also made to use FTIR for in-situ emissivity measurements, with the additional heated stage module. Figure 15 shows a schematic for this apparatus. The circular sample is mounted at the centre of the heater block and instrumented with thermocouple (TC). The sample is heated through conduction from the heater block, and the thermal radiation by the sample is directed through a series of off axis parabolic mirrors into the detection port of the FTIR (indicated by solid arrows in Figure 15(a)). A blackbody cavity is used as the reference sample, which can be set at a specific temperature (within the equipment capability) to mimic blackbody emission at that temperature. By moving the retractable mirror, it switches an alternative optical path, directing the reference sample emission into the detection port (dashed red arrows in Figure 15(a)). At each measurement temperature, a sample measurement as well as reference measurement is taken. The sample intensity signal, S_{sample}, is divided by the blackbody reference intensity signal, S_{BB}, to obtain the spectral emissivity of the sample at the temperature,

$$\varepsilon_{\lambda}(T) = \frac{S_{sample}(\lambda, T)}{S_{BB}(\lambda, T)}. \tag{3-13}$$

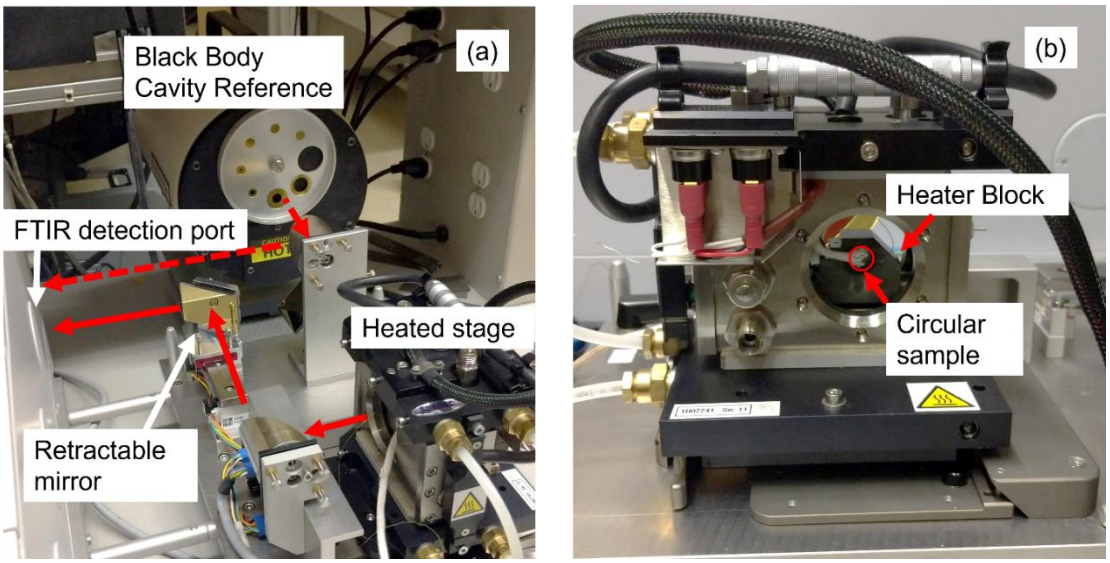

Figure 15: Heated stage module attached to the FTIR: (a) shows the overall apparatus. The red arrows illustrate the optical paths of the sample (solid line) or reference (dashed line) into the detector. The retractable mirror moves down to allow the proper optical path for reference measurements; (b) shows a close-up of the heated stage, the circular sample is mounted in the middle of the heater block.

However, the current experimental apparatus has some key limitations. Firstly, the heating power of the heater block is very limited. It can only heat the sample at a maximum rate of 0.5 ℃/s, and the heating rate tends to drop off significantly after the sample temperature exceeds 600 ℃. Eventually the sample temperature plateaus at around 680 ℃. In addition, the heating control is based on the feedback from heater block temperature, not the sample temperature. (The sample is instrumented with a thermocouple, but this thermocouple is not part of the heated cell control scheme). This leaves little control over the heating schedule since the heater controller does not receive the sample temperature. Even at maximum power, the heating condition is not close to the typical roller hearth furnace environment. It has lower heating rate (0.5 ℃/s comparing to the typical > 2 ℃/s heating rate for a roller hearth furnace during the transformation of the coating), and lower maximum sample temperature (680 ℃ comparing to the > 900 ℃ furnace set-point for a blank heated in the furnace). Since heating rate has critical influence on the coating morphology and transformation process [79], this brings scepticism to the validity to the measurement.

Secondly, the measurement range of the current set-up is also limited, only from 2 to 25 μm, missing the very important shorter wavelength from 0.5 to 2 μm, which is an essential part of the weighted integration to find total emissivity and absorptivity using Eqs. (3-9) and (3-11).

Figure 16 shows several spectral emissivity measurements at different temperatures from a continuous heating run in the heated stage. The heater is set to maximum power; a measurement is made every 15 seconds, and the sample temperature is recorded. Trends similar to those seen in Figure 14 can be observed where the spectral emissivity drops after the coating melt (from pre-melting at 555 ℃ to partially melted at 575℃, and fully melted at 630℃), and then increases gradually as the coating resolidifies and becomes rougher (675 to 681 ℃). When the coating has fully transformed, the spectral emissivity also converges for 682, 683, and 684℃

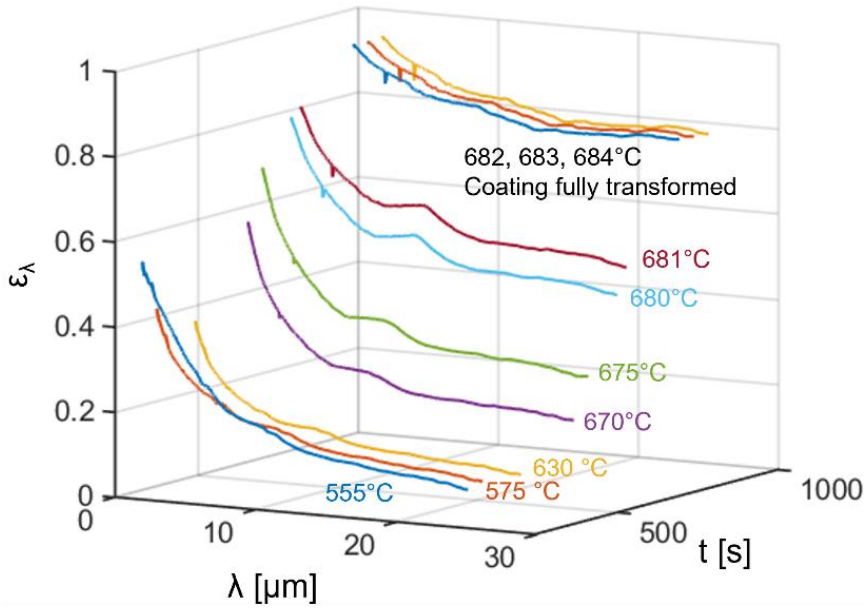

Figure 16: In-situ FTIR heated stage measurements.

While the heated stage data still provide further insight into the evolution of the coating, the heated stage apparatus in its current form has limited applicability to industrial furnaces. Several future improvements can be made to achieve the full potential of this apparatus. Firstly, a more powerful heating method with control feedback based on sample temperature; Secondly, tuning of the detector to cover the shorter wavelength. In its current state, the shorter wavelength (from 0.5 to 2 μm) data is too noisy to be usable.

3.3. Austenitization Submodels

Three candidate austenitization submodels are introduced in this section: the simplest F1 model by Di Ciano et al. [38] which is a two-DOF empirical model; the more detailed four-DOF ISV model by Huang et al. [42] which considers the effect of heating rate, temperature and existing austenite; and the phenomenological model by Li et al. [39], which considers the nucleation, growth and impingement effect of austenite.

3.3.1. F1 Model (M_1)

First-order kinetics (F1) models are a subtype of the Avrami (or Johnson–Mehl–Avrami–Kolmogorov, JMAK [84, 85]) model class, in which

$$x(t) = 1 - \exp\left(-Kt^n\right), \tag{3-14}$$

where x is the austenite fraction at time t, n is a parameter related to nucleation and growth rate, K is a temperature-dependent parameter given by the Arrhenius equation [86]

$$K = A\exp\left(-\frac{E_a}{RT}\right), \tag{3-15}$$

A is the pre-exponential factor in 1/s, E_a is the activation energy in J/mol·K, T is the temperature in K, and R = 8.314 J/mol·K is the universal gas constant. In the first-order model, n = 1. Rewriting Eq. (3-14) in differential form gives [87]

$$\frac{dx}{dt} = nK^{1/n}(1-x)\left[\ln(1-x)^{-1}\right]^{(n-1)/n}. \tag{3-16}$$

Di Ciano et al. [38] modified the equation and derived the model parameters for 22MnB5 steel. With n = 1, the model is defined as

$$\frac{df_\gamma}{dt} = A\exp\left(-\frac{E_a}{RT}\right)\left(1-f_\gamma\right), \tag{3-17}$$

where f_γ is the volume fraction of austenite and A and E_a are the two adjustable model parameters. This expression only applies when the temperature reaches a prescribed onset austenitization

temperature (T_{Ac1}), prior to which the rate of transformation is zero. The differential equation can then be solved to predict the full transformation process based on the given temperature history from the experimental data.

3.3.2. ISV Model (M_2)

Huang et al. [42] derived an ISV model for 60Si2CrA steel, based on the work by Grong et al. [88] and Cai et al. [56]. The ISV model breaks down the austentization process into an incubation period, which determines T_{Ac1}, followed by a transformation period (f_γ) over which austenitization takes place [42]. The incubation period is described by Eq. (3-18),

$$\frac{ds}{dt} = A(1-s)^B \left(\frac{dT}{dt}\right)^C \left(\frac{T}{T_{A1}} - 1\right)^E \quad (T \geq T_{A1}), \tag{3-18}$$

where A is the fitting parameter that governs the overall incubation process; B, C, and E are the parameters that regulates the effect of incubation variable, S, heating rate, dT/dt [K/s], and temperature, T [K], respectively; T_{A1} = 1000 [K] is the A_1 line of iron carbon phase diagram. The incubation process starts when T reaches T_{A1}, with s = 0, and ends when s = 1, at which point the current temperature T is the predicted T_{Ac1}. After this the austenitization process commences, described by Eq. (3-19),

$$\frac{df_\gamma}{dt} = D\left(\frac{T}{T_{Ac1}} - 1\right)^F (1-f_\gamma)^G \left(\frac{dT}{dt}\right)^H \quad (T \geq T_{Ac1}), \tag{3-19}$$

where $(1 - f_\gamma)$ represents the amount of material still available for transformation; D represents the effect of the temperature on the diffusion rate of carbon in the steel; and F, G, and H are unitless rate parameters, regulating the effect of temperature, existing austenite, and heating rate, respectively. The quantities D, F, G, and H are fitting parameters.

For the purpose of this work, only the austenitization period is adopted. There are two main reasons for this: firstly, s is not a measurable quantity (unlike the austenitization process, which can be inferred from dilatometry from start to finish), which leaves the final T_{Ac1} the only basis for fitting the model parameters. Fitting four parameters of a complicated non-linear process with only the final T_{Ac1} represents an ill-posed problem, so the outcome result might be unreliable. Secondly,

when comparing the different candidate models, it is important to keep the conditions similar. In this case that means having all the candidate models start at the same prescribed T_{Ac1}.

3.3.3. Phenomenological Model (M_3)

Li et al. [39] proposed a detailed phenomenological austenitization model, which explicitly considers nucleation and growth stages, as well as the impingement effect of existing austenite. Li et al. theorized that, under the heating rate of typical hot stamping process, austenite nucleates only in pearlite, because typical heating rates in furnaces are insufficient for carbon to diffuse to pro-eutectoid ferrite and form nucleation sites. Therefore, this model envisions the austenite process as consisting of two successive phases: a stage before the pearlite has fully transformed into austenite and one for subsequent austenitic grain growth. The model is given by a set of coupled equations that model: the nucleation rate,

$$\dot{N} = \begin{cases} A_1\left(A + \dot{T}^{\varphi_A}\right)\exp\left(-\dfrac{Q_N}{RT}\right) & \left(f_\gamma \le f_\mathrm{p}\right) \\ 0 & \left(f_\gamma > f_\mathrm{p}\right) \end{cases}, \tag{3-20}$$

where N is the number density of nuclei; the volume growth rate,

$$\dot{v} = B_1\left(B + \dot{T}^{\varphi_B}\right)\exp\left(-\frac{Q_v}{RT}\right); \tag{3-21}$$

the extended austenite growth rate (the theoretical amount of austenite formed when assuming all nuclei grow at the same rate under the same thermal conditions without impingement), given by the product of the number density of nuclei and their growth rate,

$$\dot{f}_\gamma' = N\dot{v}; \tag{3-22}$$

and the real austenite growth rate corrected for impingement effect,

$$\dot{f}_\gamma = \frac{\left(1 - f_\gamma^{\,m}\right)\dot{f}_\gamma'}{\left(1 + f_\gamma'\right)^n}, \tag{3-23}$$

where

$$m = \begin{cases} 1 & \left(f_\gamma \le f_\mathrm{p}\right) \\ 1 - m_0\left(f_\gamma - f_\mathrm{p}\right) & \left(f_\gamma > f_\mathrm{p}\right) \end{cases}, \tag{3-24}$$

$$n = n_0 \dot{f}_\gamma^{\varphi_n}, \tag{3-25}$$

and f_p is the amount of pearlite in the as-received state ($f_\mathrm{p} \approx 0.2$ for this particular material [20]). Overall, there are 11 model parameters: A_1, A, φ_A, Q_N, B_1, B, φ_B, Q_v, m_0, n_0, and φ_n. In practice, as A_1 and B_1 appear as a product, A_1B_1, they cannot be distinguished during inference and are considered a single fitting parameter. This leaves the model with 10 parameters.

3.4.Numerical Solver

As illustrated in Figure 11, based on the inputs, the time each blank spends in the furnace is calculated and discretized into time steps, such that at each time step, the theoretical location of the blank within the furnace is known, hence the heating environment is defined.

The heat transfer submodels described by the differential equations (Eq. (3-1), (3-2), and (3-8)), are coupled with a selected candidate austenitization submodel described in Sec. 3.3. The coupled differential equations are solved using the explicit Euler scheme, which predicts the temperature and austenite fraction in a stepwise manner. A grid independent solution was achieved at a time step of 0.1s.

Chapter 4 Experimental Methods and Data

Three experimental methods were used for derivation and validation of the furnace model: dilatometry experiments were conducted to collect austenitization transformations data at various heating rate; metallography tests were performed on additional samples heated to certain temperature and quenched in the dilatometry set-up as a mean of verification for the dilatometry and to provide physical insights to the transformation process; finally, roller hearth furnace trials were conducted to validate the accuracy of the overall furnace model.

4.1.Dilatometry Experiments

Dilatometry measurements were conducted using a Gleeble-3500 thermal mechanical simulator with a C-Gauge attachment. The 2 mm thick Al-Si coated 22MnB5 steel samples were cut into 150 mm x 8 mm rectangular strips, with control thermocouples (TC) welded at the centre. The C-Gauge was aligned with the TC to ensure accurate temperature feedback at the location of dilation measurement. An illustration of the experimental set-up is shown in Figure 17.

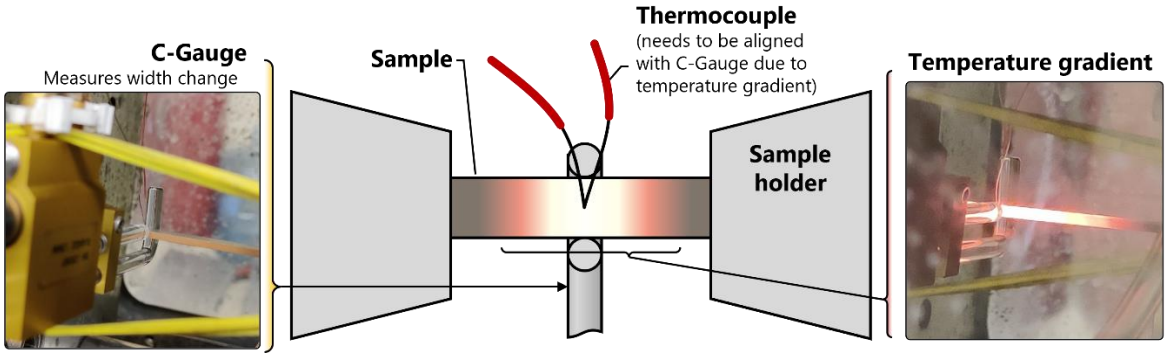

Figure 17: Gleeble dilatometry measurement set-up

The dilatometry measurements were collected at four different heating rates: 1, 2, 5, and 7 K/s, each with 5 repeated trials to quantify the uncertainties in the experimental process and aid the Bayesian model selection process. Additional samples were heated in the Gleeble at 2 and 7 K/s, to various temperatures (1043 K, 1073 K, and 1113K), then quenched rapidly to preserve the microstructure. Some of these quenched samples are used for quantitative metallography to verify

the dilatometry results, while others are examined under optical microscope to observe the different phases of transformation process. Figure 18 shows a summary of the testing scheme.

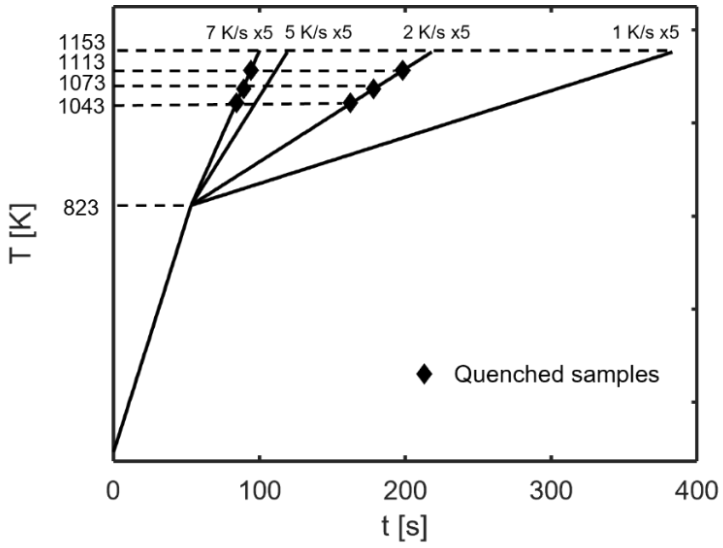

Figure 18: Test scheme of the 5 repeats per heating rate, and additional quenched trials at 7K/s and 2K/s for metallography test

The dilatometry trials measure the width dilation of the sample as it is being heated; this dilation data can be processed using a lever type rule to infer the austenitization fraction. Huang et al. [60] and Di Ciano et al. [38] detailed the use of this method, which is a standard practice for inferring austentization from in-situ dilatometry measurements. Figure 19 shows a schematic illustrating this lever rule.

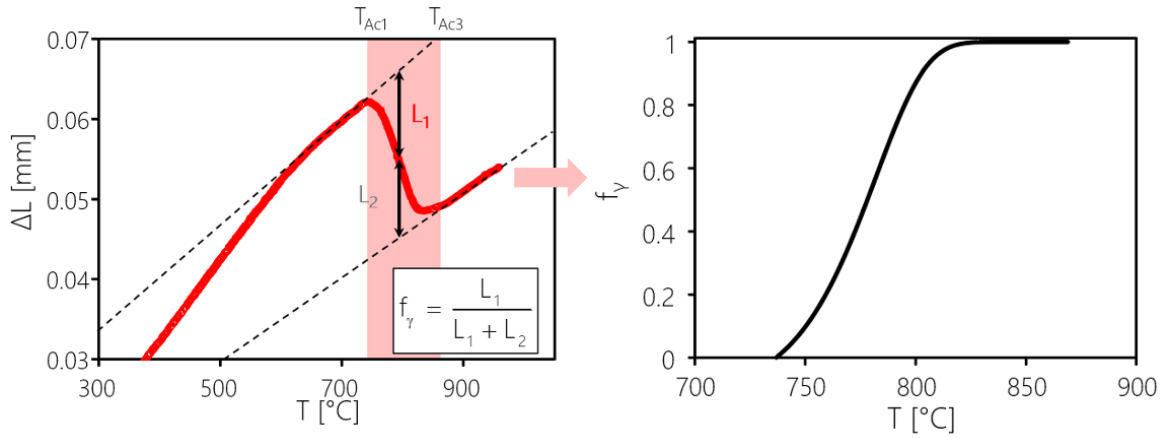

Figure 19: Schematic of the lever rule used to infer austenitization process [38]

Using the lever rule, the dilatometry results are processed and the inferred austenitization process for four heating rates as well as the average of five repeats are shown in Figure 20.

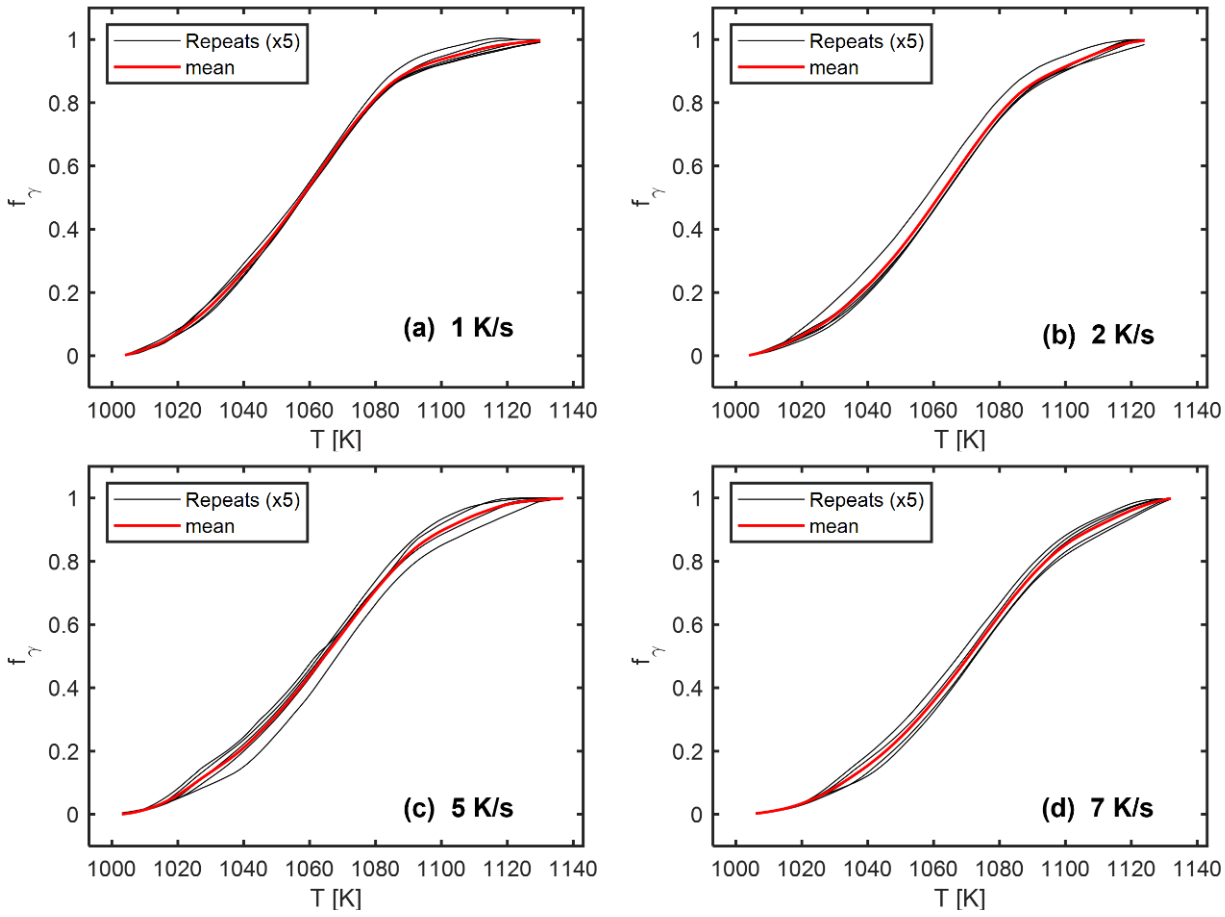

Figure 20: Inferred austenitization result at four heating rates (a) 1 K/s; (b) 2 K/s; (c) 5 K/s; and (d) 7 K/s; The mean of the five trials is also plotted to show the variation.

In addition to the above-mentioned data, the dilatometry data from the work by Di Ciano et al. [38], collected on the same material using a similar set-up, is also utilized as supplementary data. The supplementary data is used to generate priors for some candidate models. This will be discussed more in Sec. 5.3.

4.2.Metallography

As shown in the test scheme in Figure 18, some additional samples heated at 2K/s and 7K/s to designated temperatures and quenched rapidly in the Gleeble to preserve the microstructure. A

quench rate of greater than 30 K/s is delivered to ensure all present austenite at the time of extraction transforms into martensite. As an example, Figure 21 shows the microstructure evolution of as-received sample and quenched samples heated at 7K/s.

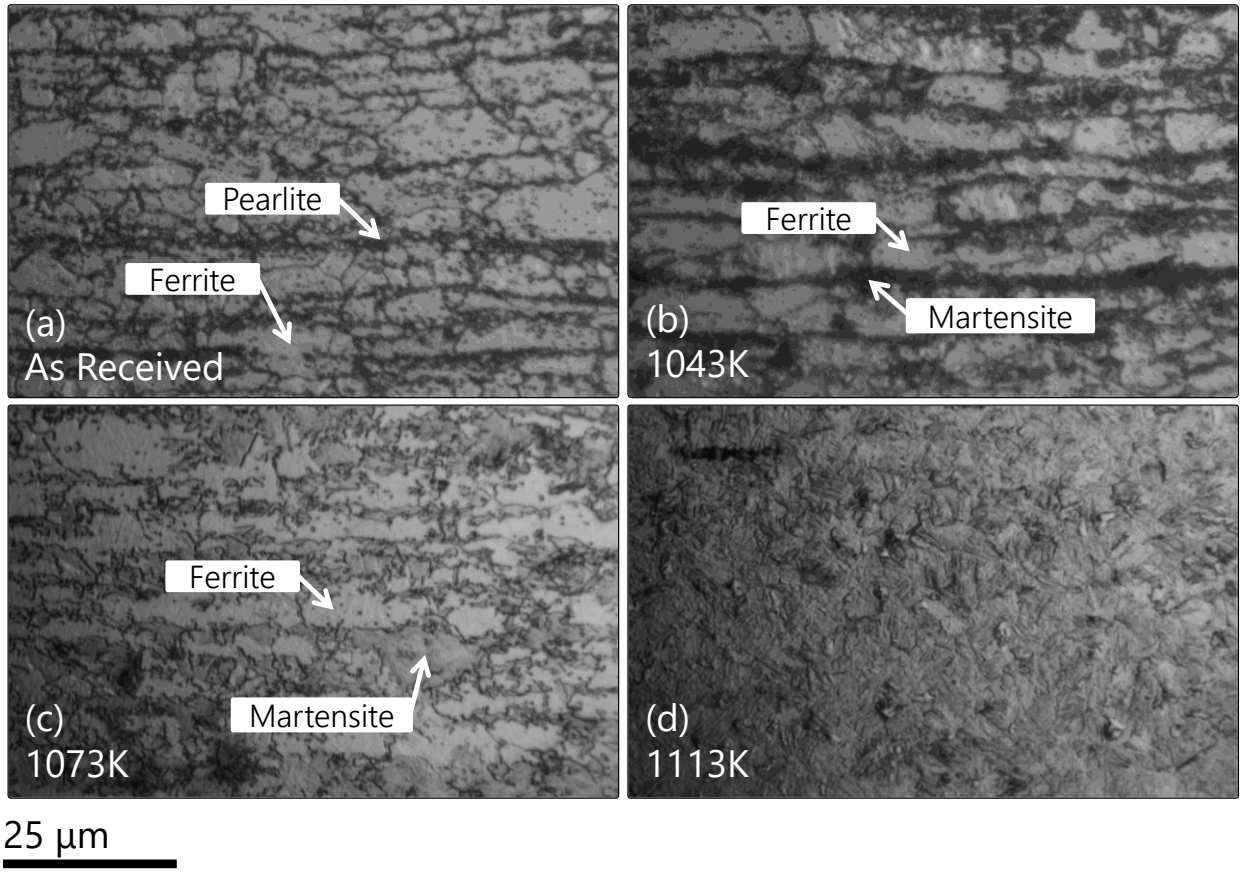

Figure 21: Optical micrographs of 22MnB5 microstructures showing: (a) as-received pearlite and ferrite mixture; samples heated to (b) 1043K; (c) 1073K; and (d) 1113K; at 7K/s heating rate and rapidly quenched in the Gleeble. The microstructure in (b) shows a small amount of martensite at previous pearlite locations, validating that pearlite transforms into austenite first [39, 63, 59], while (c) shows more ferrite transforms into martensite as the process continues, and (d) shows an almost fully martensitic microstructure. Spatial scale is identical across the panels.

Assuming volume fraction of martensite equal to the volume fraction of austenite prior to quenching, this provides a snapshot of the transformation process. Quantitative metallography techniques as per ASTM E562 [89] is used to estimate the austenite fraction at 1043K and 1073K; the results are compared in Figure 22 with the average of the inferred austenitization results shown in Figure 20.

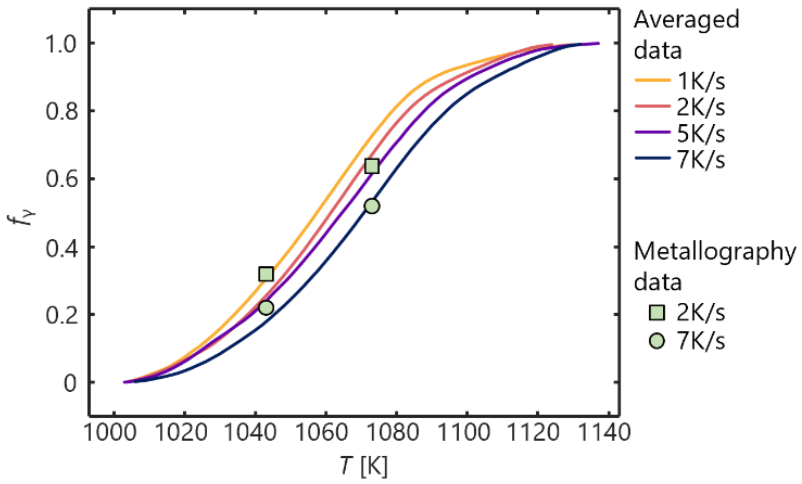

Figure 22: Average of austenite transformation at each heating rate, and results of quantitative metallography

4.3.Datapaq and Furnace Trials

In addition to dilatometry data, furnace trials were conducted in an industrial roller hearth furnace. A Datapaq® unit can be attached to the steel blank as it is travelling through the furnace to collect real-time temperature data. Figure 23 shows the Datapaq® set-up. Up to three TCs can be attached to collect measurements from different locations on the blank, while an additional TC probe exposed to the air can used to measure ambient temperature (not visible in the figure). Figure 24 shows a typical blank heating profile collected with the set-up, plotted against the derived heating rate data. From the heating rate curve, two distinct drop-offs can be identified. The first one is due to the melting of the coating, which causes the total emissivity and absorptivity to decrease, hence the drastic decrease in radiative heating. The second dip is attributed to the austenitization process, which is an endothermic process.

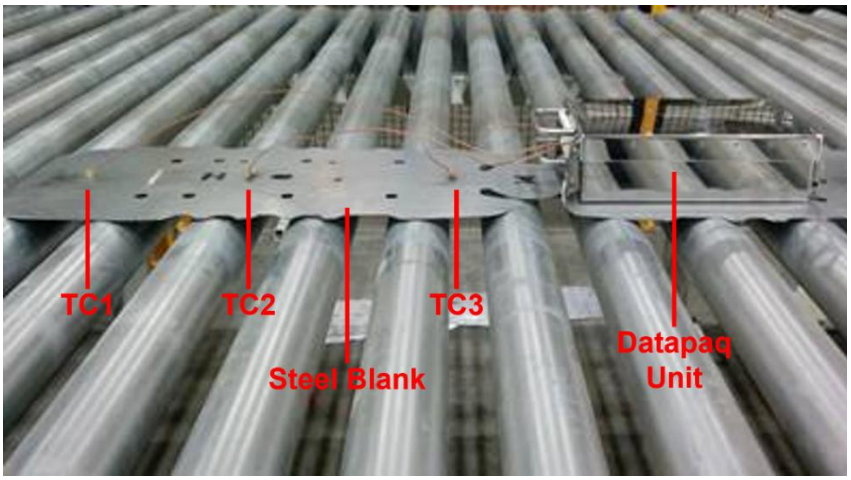

Figure 23: Schematic of Datapaq® unit attached to a blank.

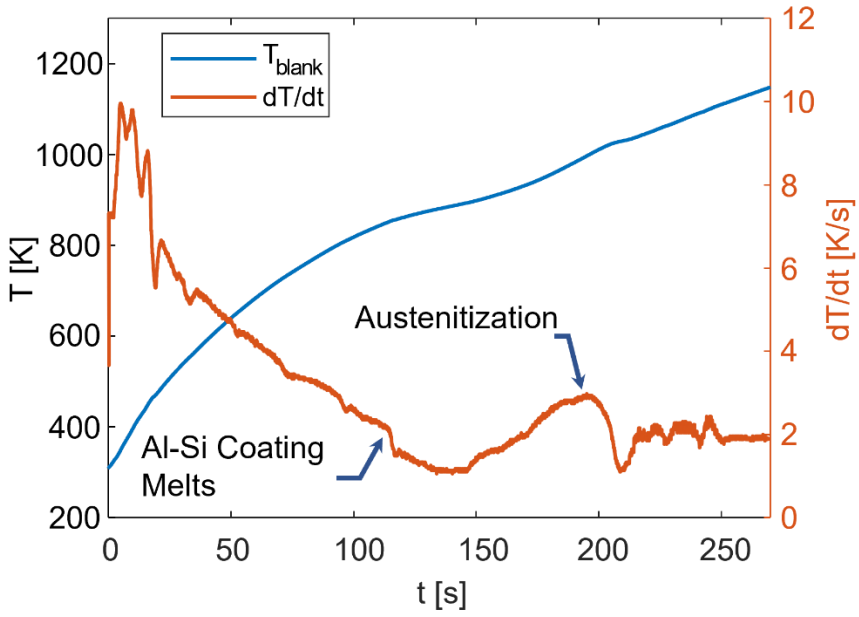

Figure 24: A typical roller hearth furnace heating profile collected using the Datapaq®. The derived heating is shown on the right axis, which shows two distinct drop-offs: one associated with the Al-Si coating liquefaction and the other related to the start of austenitization.

Chapter 5 Bayesian Model Selection Technique

Sec. 3.3 introduced three candidate austenitization submodels with varying levels of complexities. The dilatometry data collected via the procedure described in Sec. 4.1 is used to infer the parameters of these candidate models and compare their relative performances in a quantitative way. As indicated in Figure 20, certain regions of the dilatometry curves are subject to larger variances than other regions and should be viewed as "more trustworthy" when inferring the model parameters. Bayesian inference offers a statistically robust way to propagate uncertainty from the dilatometry data to uncertainties in the recovered model parameters and, subsequently, into the austenite phase fractions predicted with the model.

In this chapter, the framework of Bayesian model selection technique is introduced, including the idea of Bayesian inference, likelihood, prior, evidence, posterior, and the derivation of Baye's factor, relative credence and fit which form the theoretical basis of the model selection process; also detailed are analytical techniques used to overcome numerical hurdles (principal component analysis, PCA), procedures used to estimate missing prior information, and assumptions made to simplify the calculation; Finally, with the derived model parameters, models are compared based on their relative accuracy and complexity, and an optimal austenitization submodel is selected for the overall furnace model.

5.1.Bayesian Inference

From the Bayesian viewpoint, the data and unknown model parameters, vectors **b** and **x**, respectively, are envisioned not as "fixed" values but random variables described by probability density functions (pdfs). Within this framework, the data and quantities-of-interest (QoI) are related via

$$p_{\mathrm{po}}\left(\mathbf{x}|\mathbf{b}\right)=\frac{p\left(\mathbf{b}|\mathbf{x}\right)p_{\mathrm{pr}}\left(\mathbf{x}\right)}{p\left(\mathbf{b}\right)}\propto p\left(\mathbf{b}|\mathbf{x}\right)p_{\mathrm{pr}}\left(\mathbf{x}\right) \tag{5-1}$$

where $p_{\mathrm{po}}(\mathbf{x}|\mathbf{b})$ is the posterior pdf of **x** conditional on the observed data **b**; $p(\mathbf{b}|\mathbf{x})$ is the likelihood pdf that quantifies the likelihood that of the data given a set of model in the context of measurement noise and model error; $p_{\mathrm{pr}}(\mathbf{x})$ expresses any information about the model parameters before the

experiment (e.g. through previous experiments, physical reasoning, etc.); and $p(\mathbf{b})$ is the evidence, used to normalize the posterior pdf. The posterior concisely represents our knowledge and confidence of the model parameters given the measurement data **b** and associated uncertainties, as well as any available prior knowledge about **x**.

5.2.Likelihood

The finite width of the likelihood pdf, $p(\mathbf{b}|\mathbf{x})$ reflects the fact that the measurements and the model are fundamentally incomparable, that is

$$\mathbf{b} = \mathbf{b}^{\text{mod}}(\mathbf{x}) + \boldsymbol{\varepsilon}^{\text{meas}} + \boldsymbol{\varepsilon}^{\text{mod}} \tag{5-2}$$

where $\boldsymbol{\varepsilon}^{\text{meas}}$ and $\boldsymbol{\varepsilon}^{\text{mod}}$ are the measurement and model errors, respectively. Model error is neglected for now, while the measurement error is assumed to be unbiased and normally-distributed with a covariance matrix $\boldsymbol{\Sigma}^{\text{b}}$,

$$\varepsilon^{\text{meas}} \sim \text{N}\left(0, \boldsymbol{\Sigma}^{\text{b}}\right). \tag{5-3}$$

The likelihood is then given by,

$$p(\mathbf{b}|\mathbf{x}) = \left|2\pi\boldsymbol{\Sigma}^{\text{b}}\right|^{-1/2} \exp\left\{-\frac{1}{2}\left\|\mathbf{L}^{\text{b}}\left[\mathbf{b}^{\text{mod}}(\mathbf{x}) - \mathbf{b}\right]\right\|_2^2\right\}, \tag{5-4}$$

where $|\cdot|$ denotes the determinant, and $\mathbf{L} = \text{chol}(\boldsymbol{\Sigma}^{-1})$ is the Cholesky factorization of the inverse measurement covariance matrix. If we assume independent measurements, $\boldsymbol{\Sigma}^{\text{b}}$ will be a diagonal matrix containing the variance of each observation throughout the transformation process, and $\mathbf{L}^{\text{b}}$ will be a diagonal matrix with the inverse of the standard deviation of each observation. The Cholesky matrix, $\mathbf{L}^{\text{b}}$, serves as a weighting factor based on the confidence we have on each individual observation. For example, from Figure 20, it is evident that the start and finish of the transformation processes are relatively consistent (relatively small variance at the start and the end of $\boldsymbol{\Sigma}^{\text{b}}$), whereas more variations are present from 0.2 to 0.8 range (relatively large variance in the middle of $\boldsymbol{\Sigma}^{\text{b}}$). This, in turn, corresponds to larger values in elements at the beginning and end of $\text{diag}(\mathbf{L}^{\text{b}})$ and smaller values at the middle.

Inspection of Figure 20 reveals a second critical feature of these measurements: that the errors are highly correlated. In other words, any single realization of the data produces a curve that is likely to be consistently above or below the mean. One would expect such a feature from a continuous transformation process, since each datapoint is built upon previous data points, and therefore error will accumulate. This manifests as a highly collinear data covariance matrix, and, as a consequence, the inverse data covariance matrix, $(\mathbf{\Sigma}^{\mathrm{b}})^{-1}$, is undefined. However, the highly correlated nature of the noise also suggests that the dataset can be condensed into a more compact form, for which we use principal component analysis (PCA).

5.2.Principal Component Analysis (PCA)

PCA maps the data into a new coordinate space defined by an orthogonal set of principal components, between which there is no covariance. This is accomplished by computing the eigen-decomposition of $\mathbf{\Sigma}^{\mathrm{b}}$,

$$\mathbf{\Sigma}^{\mathrm{b}} = \mathbf{V}\mathbf{D}\mathbf{V}^{-1} = \mathbf{V}\mathbf{D}\mathbf{V}^{\mathrm{T}}, \tag{5-5}$$

where $\mathbf{D}$ is a diagonal matrix containing the eigenvalues and the column vectors of $\mathbf{V}$ are the corresponding eigenvectors. Note that, since $\mathbf{\Sigma}^{\mathrm{b}}$ is a symmetric, $\mathbf{V}$ is orthonormal (that is, $\mathbf{V}^{-1} = \mathbf{V}^{\mathrm{T}}$) and

$$\left(\mathbf{\Sigma}^{\mathrm{b}}\right)^{-1} = \mathbf{V}\mathbf{D}^{-1}\mathbf{V}^{\mathrm{T}}. \tag{5-6}$$

The eigenvectors represent the principal components, while the eigenvalues represent their significance to the data. For highly correlated data, a reduced number of principal components, k, can now be used to represent the data. In this case,

$$\mathbf{\Sigma}^{\mathrm{b}} \approx \mathbf{V}^{k}\mathbf{D}^{k}\left(\mathbf{V}^{k}\right)^{\mathrm{T}} \tag{5-7}$$

where $\mathbf{D}^{k} \in \mathbb{R}^{k\times k}$ only contains the k largest eigenvalues and $\mathbf{V}^{k} \in \mathbb{R}^{64\times k}$ (64 is the number of data points in this case) only contains corresponding eigenvectors. Within this framework, $\mathbf{V}^{k}$ represents a transformation of the original data space into one approximated by a limited number of principal components, such that

$$\mathbf{b}^{k} = \mathbf{V}^{k}\mathbf{b}, \tag{5-8}$$

which applies equally to the modeled and observed data. The covariance of the transformed data is $\mathbf{D}^k$. Substituting into the likelihood,

$$p\left(\mathbf{b}\middle|\mathbf{x}\right)=\left|2\pi\mathbf{D}^k\right|^{-1/2}\exp\left\{-\frac{1}{2}\left\|\mathbf{L}^k\left(\mathbf{V}^k\right)^{\mathrm{T}}\left[\mathbf{b}^{\mathrm{mod}}\left(\mathbf{x}\right)-\mathbf{b}^{\mathrm{obs}}\right]\right\|_2^2\right\}, \tag{5-9}$$

where $\mathbf{L}^k = \mathrm{chol}[(\mathbf{D}^k)^{-1}]$, which, given that $\mathbf{D}^k$ is diagonal, is easy to compute.

In this problem, four principal components are used to represent the data. The effectiveness of this approach is verified by generating data using $\mathbf{D}^k$ and then comparing it to the original data, **b**. As an example, Figure 25(b) shows 100 sets of simulated data and the mean of five repeats at 7K/s heating rate. The simulated data follows a similar trend, and represents the uncertainty derived from the five repeats shown in Figure 25(a).

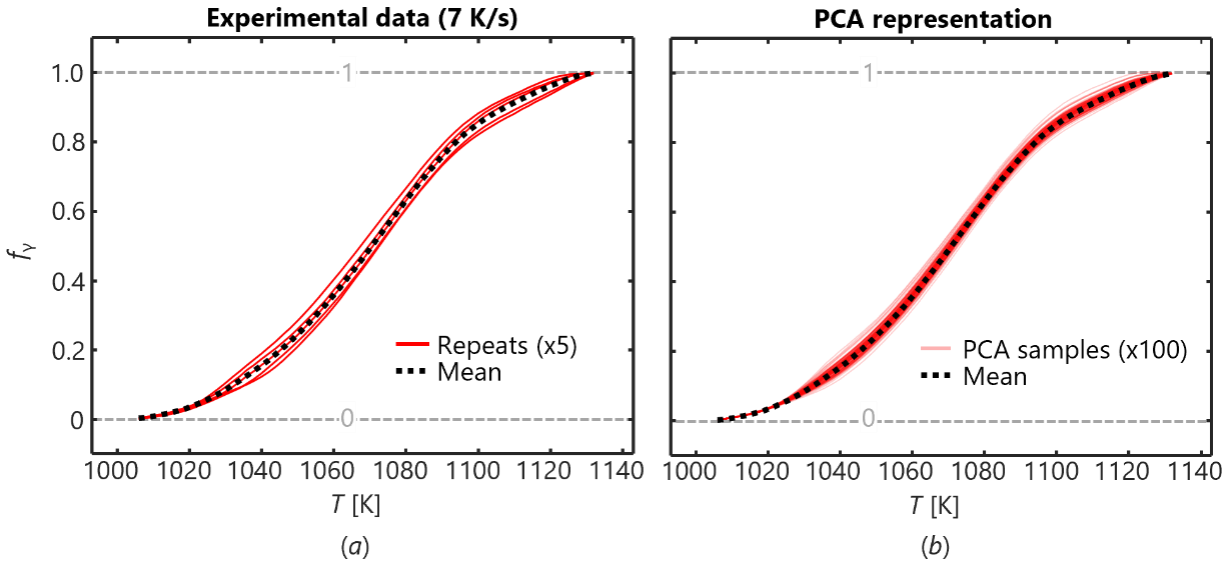

Figure 25: (a) Austenitization process for a 7 K/s (also shown in Figure 20); (b) A set of 100 random samples from the condensed covariance matrix from principal component analysis (PCA), discussed in Sec. 5.2, convert to sample data suing $\mathbf{V^k}$. Also shown is the mean of the five experimental repeats. The heating rate is 7 K/s. For (b), lines are semi-transparent, such that darker, red regions correspond to regions containing a higher concentration of PCA samples.

5.3.Prior

The prior pdf, $p_{\text{pr}}(\mathbf{x})$, contains information about the model parameters, $\mathbf{x}$, available before the measurement. This information can often be found from previous experiments in the literature, particularly when model parameters are reported with uncertainties. When defining the prior pdf, it is important to specify a prior that contributes testable information to the inference process but is otherwise as uninformative as possible to avoid unduly biasing the outcome. According to the Principle of Maximum Entropy [90], a multivariate normal distribution maximizes the information entropy, i.e., minimizes the information content in scenarios where estimates for a mean and variance/uncertainty are available. Assume a multivariate normal prior $p_{\text{pr}}(\mathbf{x})$ takes the form of

$$p_{\text{pr}}\left(\mathbf{x}\right)=\left|2\pi\boldsymbol{\Sigma}^{\text{pr}}\right|^{-1/2}\exp\left\{-\frac{1}{2}\left\|\mathbf{L}^{\text{pr}}\left(\mathbf{x}-\mathbf{x}^{\text{pr}}\right)\right\|_2^2\right\} \tag{5-10}$$

where $\boldsymbol{\Sigma}^{\text{pr}}$ is the covariance matrix of prior model parameters, $\mathbf{x}^{\text{pr}}$ is the mean of prior model parameters, and $\mathbf{x}$ is the current model parameter. For example, Di Ciano et al. [38] reported the F1 model (M_1) parameters to be normally-distributed with

$$\mathbf{x}^{\text{pr}}=\begin{bmatrix}E_{\text{a}}\\ \log_{10}A\end{bmatrix}=\begin{bmatrix}402\\ 18.5\end{bmatrix},\qquad \boldsymbol{\Sigma}^{\text{pr}}=\text{diag}\left(\begin{bmatrix}24.83\\ 1.29\end{bmatrix}\right)$$

where $\mathbf{x}^{\text{pr}}$ is the mean of model parameter vector, $\mathbf{x}$, E_{a} is in kJ/mol·K and A is in $\log_{10}\text{s}^{-1}$. These model parameters and uncertainties are derived from dilatometry data of a similar 22MnB5 steel, and therefore can be used directly as prior information in our analysis.

For some models, however, prior information of the model parameters is not readily available. In most cases, model parameters are reported as a single set of values that provide the best fit to the data without any consideration of uncertainty. Moreover, model parameters generally pertain to a particular alloy, and cannot readily be adapted to different materials. Neither the ISV model (M_2) [42] nor the phenomenological model (M_3) [39] include model parameter uncertainties, and the ISV model parameters reported by Huang et al. [42] are derived for different materials.

Accordingly, instead of using model parameters for M_2 and M_3 reported in the literature, priors are inferred from the same dilatometry data that Di Ciano et al. [38] used to obtain the M_1 model

parameters for 22MnB5 steel. The data set contains five repeats for each of the five heating rates (1, 2, 5, 10, 20 K/s). Figure 26 shows an illustration of this idea.

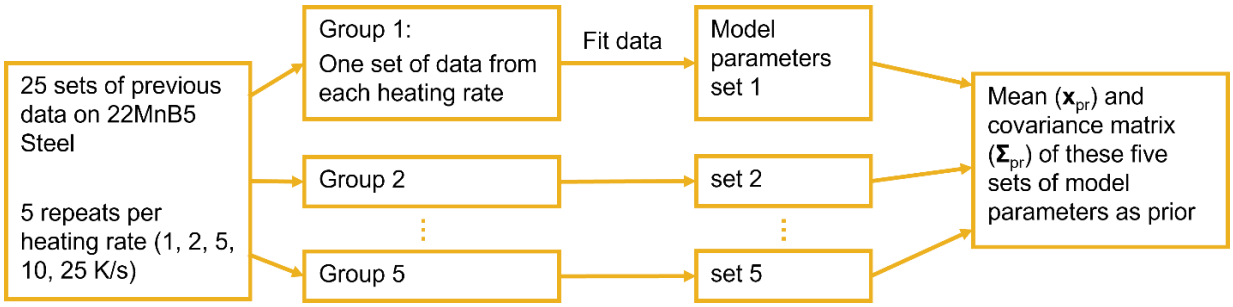

Figure 26: Schematic explaining how the prior model parameters were generated using previous dilatometry data of 22MnB5.

These 25 datasets are randomly sorted into five groups, each group containing one set of every heating rate, in order to ensure each heating rate is equally represented in every group. Note that this is not the same data used in the model selection procedure, which is introduced in Sec. 4.1. Therefore, this procedure will not introduce any bias to the analysis. Both M_2 and M_3 are fit to the five groups of data using non-linear least-squares minimization, resulting in five sets of model parameters for each model. These five sets of parameters can then be used to find mean and standard deviation of each parameter. The model parameters inferred through this process are expected to be highly correlated; however, in this work they are modeled as independent, which provides a conservative estimate of the prior pdf. With the assumption of independent model parameters, the prior pdf is fully specified by the mean, $\mathbf{x}^{pr}$ and prior covariance, $\mathbf{\Sigma}^{pr}$, similar to that of M_1. These parameters are summarized in Table 3 for M_2 and Table 4 for M_3.

Table 3: Prior information of M_2

Parameter	Prior [μ, σ]
D (-)	[0.28, 0.11]
F (-)	[0.89, 0.10]
G (-)	[0.59, 0.06]
H (-)	[0.96, 0.06]

Table 4: Prior information of M_3 and comparison to reported values

Parameter	Prior [μ, σ]	Reported value
A_1B_1(kJ/mol)	[2.20×10^4, 2.22×10^3]	2.39×10^3
A (-)	[0.12, 0.001]	0.80
φ_A (-)	[1.92, 0.17]	1.41
Q_N (kJ/mol)	[29.02, 9.21]	148.6
B (-)	[9.36, 0.81]	1
φ_B (-)	[0.32, 0.45]	0.12
Q_v (kJ/mol)	[203.08, 10.95]	40.5
m_0 (-)	[0.16, 0.01]	1.05
n_0 (-)	[8.35, 7.35]	2.1
φ_n (-)	[1.54, 0.005]	0.155

Also listed in Table 4 are the reported values of model parameters by Li et al. [39], which differ significantly from the ones found using Di Ciano et al.'s data [38], even though both experiments follow similar procedures and were carried out on similar material. This may be an indication of over-tuning, and further highlights the important role of model complexity as a crucial criterion in model evaluation and comparison.

5.4.Evidence and Posterior

The evidence, $p(\mathbf{b})$, represents the probability density of observing the data vector $\mathbf{b}$, and is found from

$$E = p(\mathbf{b}) = \int_{\mathbf{x}} p(\mathbf{b}|\mathbf{x})\, p_{pr}(\mathbf{x})\, d\mathbf{x} \tag{5-11}$$

Substituting this result into Eq. (5-1), along with the likelihood and prior pdfs, results in an expression for the posterior pdf for the model parameters, $p_{po}(\mathbf{x}|\mathbf{b})$.

The posterior pdf is a joint probability density with a dimension equal to the number of model parameters; for model M_1, $p(\mathbf{x}|\mathbf{b})$ can be visualized as a contour or surface plot, but this cannot be

done for M_2 and M_3, which have more than two parameters. Instead, the posterior pdf is often summarized by the maximum a posteriori (MAP) estimate, $\mathbf{x}^{\text{MAP}}$. With the assumption of normal likelihood and prior, $\mathbf{x}^{\text{MAP}}$ can be calculated as

$$\mathbf{x}^{\text{MAP}} = \arg\max_{\mathbf{x}} \left\{ p_{\text{po}}\left(\mathbf{x}|\mathbf{b}\right)\right\} = \arg\min_{\mathbf{x}} \left\{ \left\| \mathbf{L}^{k}\left(\mathbf{V}^{k}\right)^{\text{T}}\left[\mathbf{b}^{\text{mod}}\left(\mathbf{x}\right)-\mathbf{b}\right]\right\|_2^2 + \left\|\mathbf{L}^{\text{pr}}\left(\mathbf{x}-\mathbf{x}^{\text{pr}}\right)\right\|_2^2 \right\} \quad (5\text{-}12)$$

Evaluating $p_{\text{po}}(\mathbf{x}|\mathbf{b})$ requires calculating the evidence, which is a computationally intensive process. Instead, if the posterior is modeled as Gaussian (i.e. $\mathbf{b}^{\text{mod}}(\mathbf{x})$ is approximately linear close to $\mathbf{x}^{\text{MAP}}$), Laplace's approximation may be used [91, 92]

$$p_{\text{po}}\left(\mathbf{x}|\mathbf{b}\right) = \left|2\pi\boldsymbol{\Sigma}^{\text{po}}\right|^{-1/2} \exp\left\{-\frac{1}{2}\left\|\mathbf{L}^{\text{po}}\left[\mathbf{x}-\mathbf{x}^{\text{MAP}}\right]\right\|_2^2\right\} \quad (5\text{-}13)$$

The posterior covariance matrix, $\boldsymbol{\Sigma}^{\text{po}}$, is calculated using

$$\boldsymbol{\Sigma}^{\text{po}} = \left[\mathbf{L}^{\text{po}}\left(\mathbf{L}^{\text{po}}\right)^{\text{T}}\right]^{-1} = \left[\mathbf{J}^{\text{T}}\left(\boldsymbol{\Sigma}^{\text{b}}\right)^{-1}\mathbf{J} + \left(\boldsymbol{\Sigma}^{\text{pr}}\right)^{-1}\right]^{-1} = \left[\left(\mathbf{V}^{k}\mathbf{J}\right)^{\text{T}}\left(\mathbf{D}^{k}\right)^{-1}\mathbf{V}^{k}\mathbf{J} + \left(\boldsymbol{\Sigma}^{\text{pr}}\right)^{-1}\right]^{-1} \quad (5\text{-}14)$$

and $\mathbf{J}$ is the Jacobian matrix, having elements equal to

$$J_{ij} = \frac{\partial b_i^{\text{mod}}}{\partial x_j}, \quad (5\text{-}15)$$

and evaluated at $\mathbf{x}^{\text{MAP}}$. The Jacobian can be directly obtained as a by-product of the nonlinear least-squares minimization algorithm used to find $\mathbf{x}^{\text{MAP}}$. In this case, $\mathbf{x}^{\text{MAP}}$ represents a point estimate of the derived model parameters (recall that in Bayesian point of view, model parameters are pdfs rather than a definitive set of numbers), and it's also the mean of the pdf that describes the model parameters, i.e., $\boldsymbol{\mu}$. The mean and $\boldsymbol{\Sigma}^{\text{po}}$ together define the distribution of model parameters, in which case $\boldsymbol{\Sigma}^{\text{po}}$ represents the uncertainties associated with the mean. For example, for the F1 Model,

$$\boldsymbol{\mu}^{\text{F1}} = \mathbf{x}^{\text{MAP,F1}} = \begin{bmatrix} x_1 \\ x_2 \end{bmatrix} = \begin{bmatrix} E_{\text{a}} \\ \log_{10} A \end{bmatrix} = \begin{bmatrix} 444.84 \\ 20.84 \end{bmatrix}; \qquad \boldsymbol{\Sigma}^{\text{po,F1}} = \begin{bmatrix} \sigma_{E_a}^2 & \sigma_{E_a,\log_{10}A}^2 \\ \sigma_{E_a,\log_{10}A}^2 & \sigma_{\log_{10}A}^2 \end{bmatrix} = \begin{bmatrix} 2.6882 & 0.1318 \\ 0.1318 & 0.0065 \end{bmatrix},$$

One could visualize the pdf function for a particular parameter by marginalizing over all the other parameters and constructing the credible intervals (CI). Say, a model has *n* parameters, i.e., $\mathbf{x}^{MAP} \in \mathbb{R}^{n\times 1}$. $p(x_j|\mathbf{b})$ can be found by,

$$p\left(x_j \mid \mathbf{b}\right) = \int_{x_1}\int_{x_2}\cdots\int_{x_{j-1}}\int_{x_{j+1}}\cdots\int_{x_n} p\left(\mathbf{x}\mid\mathbf{b}\right) dx_1 dx_2 \cdots dx_{j-1} dx_{j+1} \cdots dx_n. \tag{5-16}$$

As and example, for F1 model, $p(E_a)$ can be found through,

$$p\left(E_a\right) = p\left(x_1 \mid b\right) = \int_{x_2} p\left(x \mid b\right) dx_2.$$

This marginalization process can be mathematically cumbersome, but under the assumption of normally distributed measurement error and linear model, the resultant marginalized pdf is also Gaussian. Therefore, as an example, $p(E_a)$ and its CI can be visualized in Figure 27.

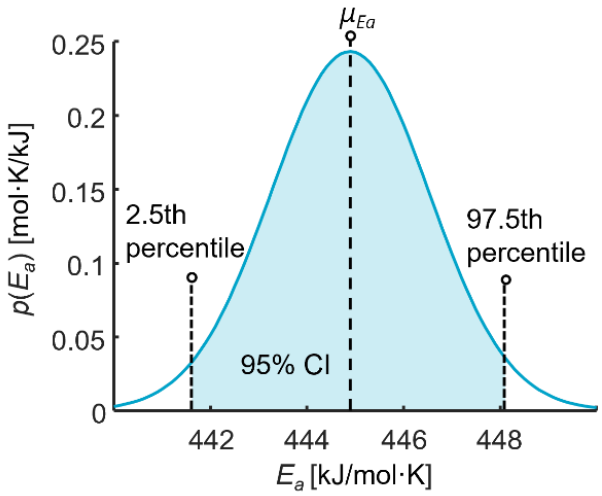

Figure 27: Marginalized pdf of E_a, demonstrating the 95% credible interval (CI).

Note that this is only an approximate case, under the assumption of Gaussian measurement error and linear model. In reality, the model is only linear near $\mathbf{x}^{MAP}$ and not linear near the tail end of the distribution. In order to find the true marginalized distribution, one would need to fully carry out the integration in Eq. (5-16), which is mathematically challenging but can be done with numerical integration schemes such as Markov chain Monte Carlo (MCMC) technique.

5.5.Bayes' Factor, Measurement Credence and Fit

The posterior probability density derived through Eq. (5-1) accounts for the measurement covariance through the conditional probability $p_{\mathrm{po}}(\mathbf{x}|\mathbf{b})$, but there is an additional "hidden" dependency on the choice of model, i.e. $p_{\mathrm{po}}(\mathbf{x}|\mathbf{b}) = p_{\mathrm{po}}(\mathbf{x}|\mathbf{b},M_i)$ where M_i is the measurement model. Eq. (5-1) then transforms into

$$p_{\mathrm{po}}\left(\mathbf{x}_i|\mathbf{b},M_i\right)=\frac{p\left(\mathbf{b}|\mathbf{x}_i,M_i\right)p_{\mathrm{pr}}\left(\mathbf{x}_i|M_i\right)}{p\left(\mathbf{b}|M_i\right)}=\frac{p\left(\mathbf{b}|\mathbf{x}_i,M_i\right)p_{\mathrm{pr}}\left(\mathbf{x}_i|M_i\right)}{E_i}, \tag{5-17}$$

where E_i is the evidence conditional on model M_i, which marginalizes over the model parameters.

Suppose, as in this case, there exists a manifold of candidate models, $\{M_i\}\ \forall\ i \in \{1, 2, \ldots m\}$. The model posterior probability, i.e., the probability that M_i is the model that produced the observed data, can be stated using another instance of Bayes' equation

$$p_{\mathrm{po}}\left(M_i|\mathbf{b}\right)\propto p\left(\mathbf{b}|M_i\right)p_{\mathrm{pr}}\left(M_i\right)=E_i p_{\mathrm{pr}}\left(\mathrm{M}_i\right), \tag{5-18}$$

where $p(\mathbf{b}|M_i)$ is the model likelihood, indicating the probability density of observing the data $\mathbf{b}$ using model M_i, and $p_{\mathrm{pr}}(M_i)$ is the model prior, which describes the prior probability of a given model based on what is known before the measurement. We note that the model likelihood is the same as the evidence from Eq. (5-11) and thus involves a marginalization over the model parameters. Note the distinction between model prior, $p_{\mathrm{pr}}(M_i)$, and prior pdf on model parameter, $p_{\mathrm{pr}}(\mathbf{x}|M_i)$; the model parameter prior can often be obtained either from the literature or through previous experiments as detailed in Sec.5.3, whereas the model prior is often set equal to unity, when no model is preferred. With this assumption Eq. (5-18) becomes

$$p_{\mathrm{po}}\left(M_{\mathrm{i}}|\mathbf{b}\right)\propto E_i. \tag{5-19}$$

A major challenge in assessing the model posterior probability concerns calculating the model evidence. In order to calculate a "true" evidence, however, the entire set of candidate models would need to be marginalized. Instead, it is often sufficient to calculate the relative model posteriors, i.e. $P_{\text{po}}(M_i|\mathbf{b})/P_{\text{po}}(M_j|\mathbf{b})$. If the model priors are taken to be unity, this becomes the Bayes factor,

$$B_{ij} = \frac{p_{\text{po}}\left(M_i|\mathbf{b}\right)}{p_{\text{po}}\left(M_j|\mathbf{b}\right)} = \frac{p\left(\mathbf{b}|M_i\right)}{p\left(\mathbf{b}|M_j\right)} = \frac{E_i}{E_j}, \tag{5-20}$$

which describes the odds that M_{i} produces the data $\mathbf{b}$ over M_{j}. A positive B_{ij} indicates that model M_i is preferred over model M_j. Furthermore, Eq. (5-17) can be rearranged into

$$E_i = \frac{p\left(\mathbf{b}|\mathbf{x}_i, M_i\right) p_{\text{pr}}\left(\mathbf{x}_i|M_i\right)}{p_{\text{po}}\left(\mathbf{x}_i|\mathbf{b}, M_i\right)}, \tag{5-21}$$

with the posterior probability density calculated using Laplace's approximation, Eq. (5-13). Under this assumption, the evidence is independent of $\mathbf{x}_i$; for simplicity, the terms in Eq. (5-21) evaluated at the $\mathbf{x}^{\text{MAP}}$.

For numerical stability, model selection is often done using the logarithm of the evidence, which can be further broken down into three major components [47, 93] shown in Eq. (5-22).

$$\ln\left(E_i\right) = C_i + F_{\text{b},i} + F_{\text{pr},i} \tag{5-22}$$

The measurement credence, C_i, is defined as

$$C_i = \ln\left(\left|2\pi\boldsymbol{\Sigma}_i^{\text{po}}\right|^{1/2}\right) - \ln\left(\left|2\pi\boldsymbol{\Sigma}_i^{\text{pr}}\right|^{1/2}\right) - \ln\left(\left|2\pi\boldsymbol{\Sigma}^{\text{b}}\right|^{1/2}\right); \tag{5-23}$$

The relative fit of the model to data, $F_{\text{b,i}}$, evaluated at $\mathbf{x}^{\text{MAP}}$, is defined as

$$F_{\text{b},i} = -\frac{1}{2}\left\|\mathbf{L}^{\text{b}}\left[\mathbf{b}_i^{\text{mod}}\left(\mathbf{x}_i^{\text{MAP}}\right) - \mathbf{b}^{\text{obs}}\right]\right\|_2^2; \tag{5-24}$$

and, similarly, the relative fit of $\mathbf{x}^{\text{MAP}}$ to prior, $F_{\text{pr},i}$, is defined as

$$F_{\text{pr},i} = -\frac{1}{2}\left\|\mathbf{L}_i^{\text{pr}}\left(\mathbf{x}_i^{\text{MAP}} - \mathbf{x}_i^{\text{pr}}\right)\right\|_2^2. \tag{5-25}$$

These three terms provide more insight on how well a particular model performs. The measurement credence includes determinants that normalize the posterior, prior, and likelihood densities [47]. Large determinants represent "diffuse" distributions that are highly uncertain, contain less information, or have a high number of parameters (i.e., complex models with many DOFs). A large $|\mathbf{\Sigma}^{\mathrm{po}}|$ indicates less confidence in the derived model parameters, which happens when the model is too complex with too many DOFs. This is balanced out by the information provided by the prior parameters (and the data, though this is identical across the models, and cancels out in computing the Bayes factor) and is inversely proportional to $|\mathbf{\Sigma}^{\mathrm{pr}}|$, respectively. The credence accounts for the model degrees-of-freedom through the size of $|\mathbf{\Sigma}^{\mathrm{po}}|$, though it is an oversimplification to assume that models having many DOF will necessarily have a small credence. Having many model parameters is permissible, as long as the elements of $\mathbf{\Sigma}^{\mathrm{pr}}$ are small, which is true if the prior information about the parameters is specific and reliable.

Taking the logarithm of Eq. (5-20) results in

$$\ln\left(B_{ij}\right)=\left(C_i-C_j\right)+\left(F_{\mathrm{b},i}-F_{\mathrm{b},j}\right)+\left(F_{\mathrm{pr},i}-F_{\mathrm{pr},j}\right)=\Delta C_{ij}+\Delta F_{ij}, \tag{5-26}$$

where ΔC_{ij} is the relative measurement credence and ΔF_{ij} is the relative fit. These two competing parameters weigh each model's complexity against its accuracy in a quantitative way, in the context of the prior covariance and the measurement covariance. For example, ΔC_{ij} may be positive if M_i is simpler than M_j, but ΔF_{ij} may be negative if M_j gives a better goodness-of-fit to the data, or returns a set of model parameters more in keeping with known physics. We note that $|\mathbf{\Sigma}^{\mathrm{b}}|$ cancels out in this procedure and only enters the calculation via the MAP estimate and in computing $|\mathbf{\Sigma}^{\mathrm{po}}|$.

5.6.Model Selection Results and Discussion

This procedure is used to identify the most probable austenitization submodel for 22MnB5, based on the dilatometry data discussed in Sec. 4.1. Table 5 summarizes $\mathbf{x}^{\mathrm{MAP}}$ for each model parameters obtained through minimizing Eq. (5-12) as well as their associated uncertainties.

Table 5: $\mathbf{x}^{MAP}$ and uncertainties for candidate austenitization models, [μ, σ]

***M*₁ – F1 model**	
E_a (kJ/mol·K)	[444.84, 1.63]
$\mathrm{Log}_{10} A$ ($\log_{10}\mathrm{s}^{-1}$)	[20.84, 0.08]
***M*₂ – ISV model**	
D (-)	[0.11, 0.005]
F (-)	[0.63, 0.011]
G (-)	[0.36, 0.012]
H (-)	[0.88, 0.007]
***M*₃ – Phenomenological model**	
A_1B_1(kJ/mol)	[2.39×10^4, 2.21×10^3]
A (-)	[0.12, 0.001]
φ_A (-)	[1.53, 0.049]
Q_N (kJ/mol)	[22.29, 3.626]
B (-)	[10, 0.808]
φ_B (-)	[0.86, 0.142]
Q_v (kJ/mol)	[209.32, 3.583]
m_0 (-)	[0.15, 0.012]
n_0 (-)	[0.31, 2.311]
φ_n (-)	[1.54, 0.005]

For all three candidate models, the Jacobian matrix, **J**, is acquired as a by-product of the minimization algorithm used to find $\mathbf{x}^{MAP}$, and $\mathbf{\Sigma}^{po}$ is found using Eq. (5-14). The measurement credence, C_i, is evaluated using Eq. (5-23). Both $F_{b,i}$ and $F_{pr,i}$ can be obtained easily using Eqs. (5-24) and (5-25), as both ($\mathbf{b}^{mod} - \mathbf{b}$) and ($\mathbf{x}^{MAP} - \mathbf{x}^{pr}$) have already been calculated. Subsequently, ΔC_{ij}, ΔF_{ij}, and $\ln(B_{ij})$ are evaluated from these results using Eq. (5-26) and is illustrated in Figure 28.

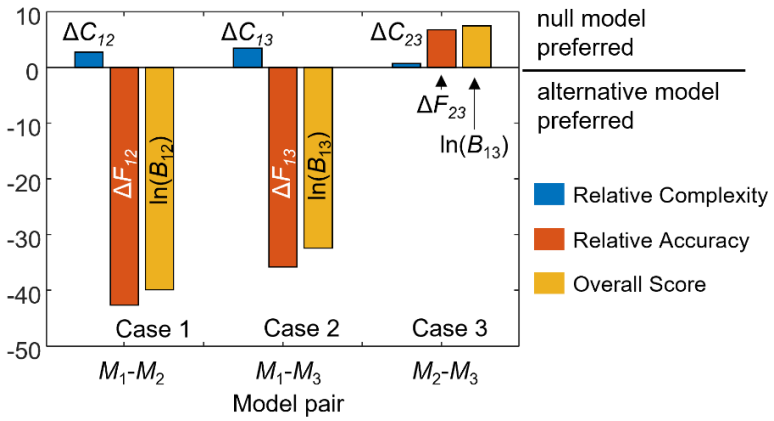

Figure 28: Model selection result visualized, M_1 is the F1 model (2 DOFs), M_2 is the ISV model (4 DOFs), and M_3 is the phenomenological model (10 DOFs). M_1's advantage in low complexity is offset by its lack in accuracy comparing to both M_2 and M_3. M_2 which best balances complexity and accuracy is selected as the optimal model.

The three models are compared in pairs by evaluating ΔC_{ij}, ΔF_{ij}, and the resulting Bayes factor, $\ln(B_{ij})$ as shown in Figure 28. We start by comparing M_2 to M_1 (Case 1) and M_3 to M_1 (Case 2). Taking M_1 to be the null model, and M_2 and M_3 are the alternative models in cases 1 and 2 respectively. Since the null model is the simplest with only two DOF, it is preferred in terms of relative measurement credence, as indicated by the positive ΔC_{12} and ΔC_{13}. However, it provides an inferior goodness-of-fit, as indicated by the negative ΔF_{12} and ΔF_{13}, suggesting that two DOFs is inadequate to capture the physical processes that underlie austenitization. This results in overall negative Bayes factors, $\ln(B_{12})$ and $\ln(B_{13})$. For Case 3, we suppose that M_2 (4 DOFs) is the preferred null model and M_3 (10 DOFs) is the alternative model. M_3 is much more complex than M_2, but the added complexity does not realize an improved goodness-of-fit. On the contrary, M_2 outperformed M_3 in both relative measurement credence and fit, and is therefore the optimal model.

Overall, this approach exemplifies the fact that Bayesian model selection technique accounts for data uncertainty, model complexity, and prior information to derive an unambiguous and statistically-rigorous indicator of model performance in the form of the Bayes factor. In comparison, the conventional approach of goodness-of-fit misses these nuances and may lead to misleading or erroneous conclusions. As an example, Figure 29 compares between three model predictions and the data (the mean of five repeats) at 5 K/s heating rate. One could determine that

M_1 is the worst of all three based solely on goodness-of-fit, but will struggle to compare M_2 and M_3 without a quantitative score (ΔF_{23}) or any insight into the model complexity and uncertainties (ΔC_{23}).

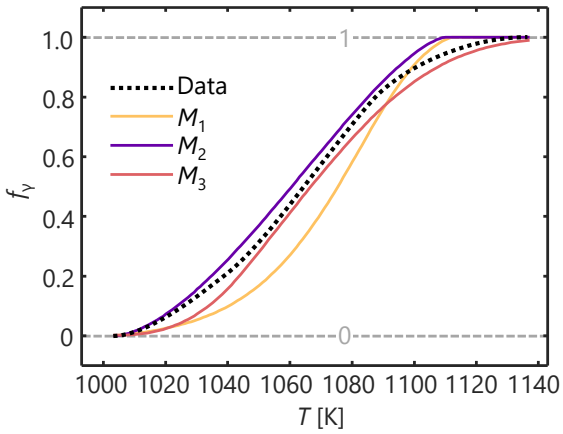

Figure 29: Comparison of three model predictions at 5 K/s heating rate. This demonstrates the poor fit between the data and M_1. It also illustrates the drawback of goodness-of-fit evaluation method, as one cannot easily determine the better model between M_2 and M_3.

Given the PCA representation of the data, one can also generate a series of artificial data that represent the range observed in the experimental data, i.e., the samples shown in Figure 25 (b). This feature could be leveraged to study the uncertainties associated with ΔC_{ij}, ΔF_{ij}, and $\ln(B_{ij})$. Supposed that 250 new random sets of data are generated. This data can then be used to repeat the model selection procedure 250 times to compute a distribution of Bayes factors, as visualized in Figure 30 for 250 samples.

The result from the experimental data, i.e., the point estimates from Figure 28, are also provided in the plots. The sampled data produce a spread of results centered around the point estimates, as expected. This exercise reflects the Bayesian viewpoint of not treating parameters as deterministic (such as the point estimate results in Figure 28) but rather as random variables that obey distributions (such as the ones in Figure 30). If the analysis is repeated with a different set of data, one may not end up with the same numbers shown in Figure 28, but it will likely lie within the distribution captured in Figure 30. This also illustrates that even with uncertainties considered, the decision of choosing M_2 as the optimal model still stands.

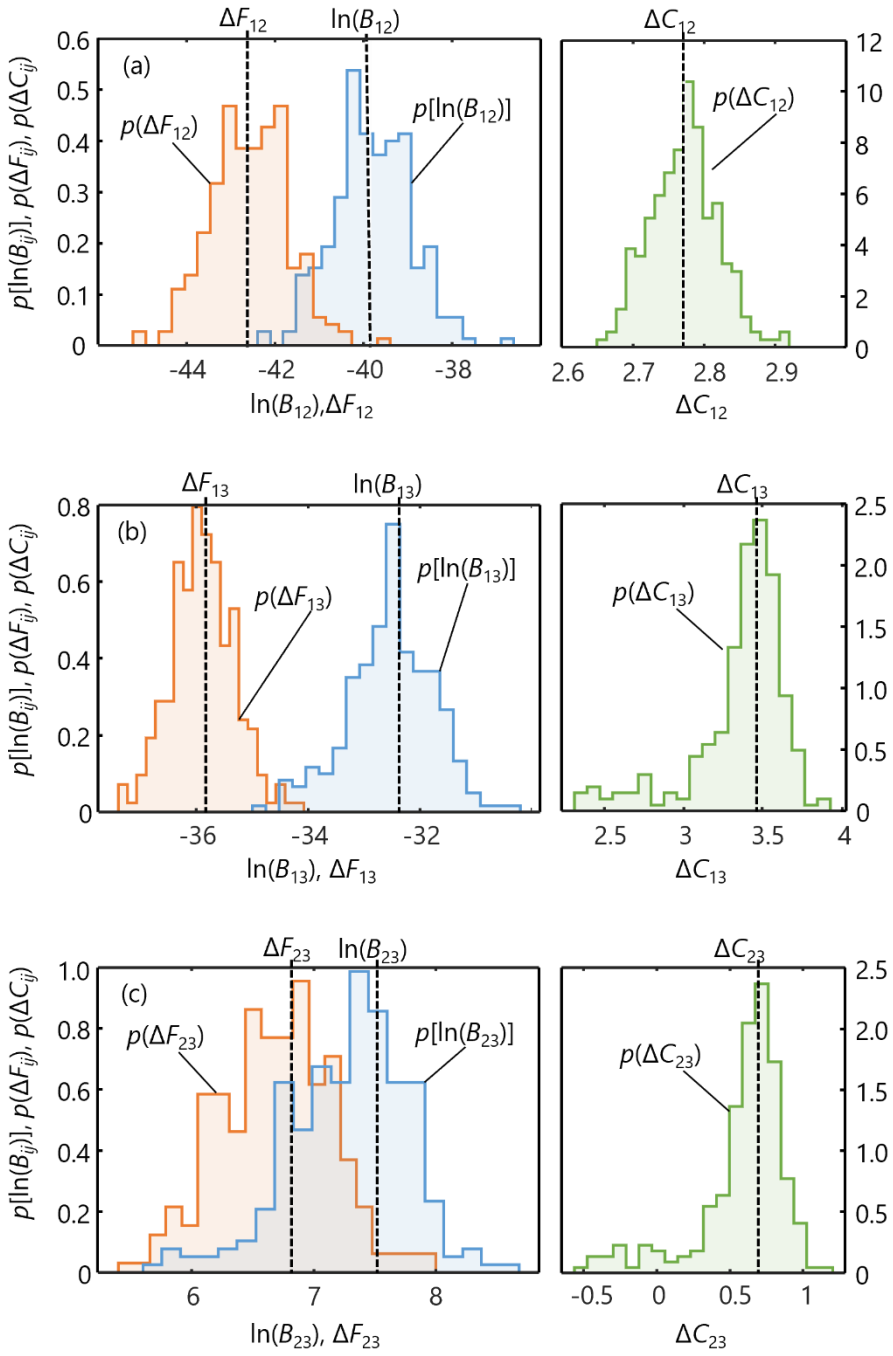

Figure 30: Histograms showing the Bayes factor and its components for 250 samples from the PCA representation of the data for (a) Case 1; (b) Case 2; and (c) Case 3. Note that ΔC_{ij} has much smaller uncertainties than ΔF_{ij}, and is plotted on a separate axis for clarity.

Chapter 6 Model Validation

The thermometallurgical model is validated using two types of data. The accuracies of austenitization submodels are compared using dilatometry data as a visual illustration, and the overall furnace model, combined with the selected austenitization submodel, is validated using roller hearth furnace trials.

6.1.Austenitization Submodels Comparison with Dilatometry Data

The Bayesian model selection technique detailed in Chapter 5 already provides a quantitative method to evaluated candidate model performances and their accuracy, while taking into consideration the uncertainties in the dilatometry data. It was concluded in Sec. 5.6 that the F1 model lacks the necessary complexity to capture the transformation process accurately. The ISV and Li's model are similar in terms of accuracy, but Li's model is much more complicated with 10 DOFs comparing to the 4 DOFs of ISV model. Its added complexity is not justified by improvements of accuracy. Therefore, ISV model is determined to be the winning candidate model that best balances accuracy and complexity. In this section, the three models are compared with the dilatometry data detailed in Sec. 4.1, to provide a more visual and qualitative comparison of their performances as a supplement to the Bayesian model selection technique. Figure 31 shows the five repeats of collected at 1, 2, 5, and 7 K/s alongside the three model predictions.

It can be observed that F1 clearly does not accurately represent the austentization process at certain heating rates. This can be attributed to its simplicity with only two DOFs. It does not explicitly consider the physical mechanism of austenitization process like Li's more physical model does. Despite both being empirical models, it also does not consider important factors that affect the transformation process, such as the heating rate, as does the ISV model. Therefore, it lacks the fine adjustment to model the effect of heating rate, and only appears to perform reasonable well for 2 K/s shown in Figure 31 (b), over predicting for 1 K/s (Figure 31 (a)), and underpredicting for both 5 and 7 K/s (Figure 31 (c) and (d)).

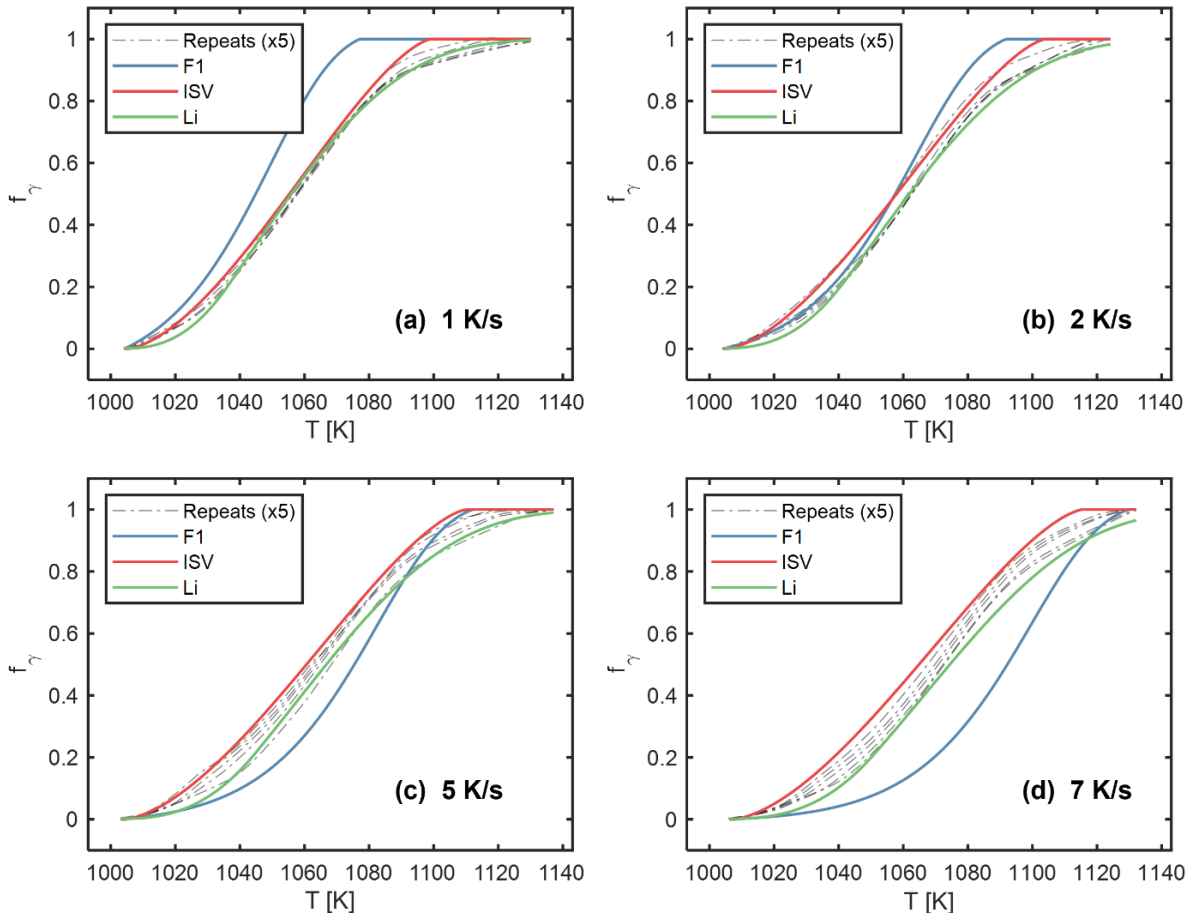

Figure 31: Qualitative comparison of dilatometry data (detailed in Sec. 4.1) against the model prediction at four different heating rates: (a) 1 K/s; (b) 2 K/s; (c) 5 K/s; and (d) 7 K/s

Simply based on qualitative observation, both the ISV and Li's model are accurate enough in comparison to the relative spread of the five repeats at each of the heating rate shown in Figure 31. This further underlines the importance of Bayesian model selection technique as a quantitative evaluation, as one would struggle to decide between ISV and Li's model without considering the data uncertainties and weighing model accuracy with complexity.

As another means for comparison, the dilatometry data collected by Di Ciano et al. [38] is also compared against the three candidate model predictions. This data is collected using a similar Gleeble 3500 Thermomechanical simulator C-gauge set-up as described in Sec. 4.1, on similar 22MnB5 steel material. The only difference between Di Ciano et al.'s work and the present work is the shape of the sample. Instead of a slim rectangular strip, Di Ciano et al. opted for a dog-boned

sample similar to a sample design used in tensile testing. Figure 32 shows the dimension of the sample design.

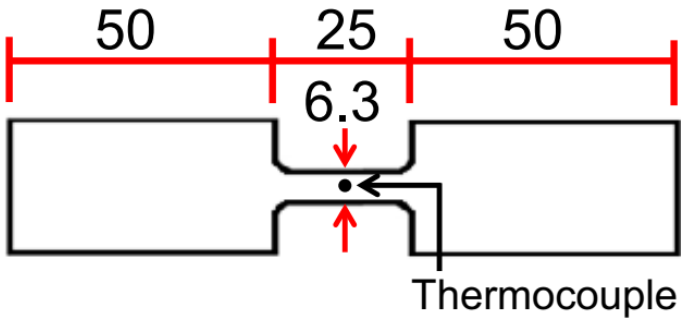

Figure 32: Drawings showing the sample dimensions used by the Di Ciano et al. [38], all units are in mm.

This design, however, is unnecessarily complex, since the dog-bone shape is not needed for a heating test. Another downside of this sample shape is the extra materials on either end will require additional power to heat up; this might worsen the already existing thermal gradient issue shown in Figure 17, especially at higher heating rates. Di Ciano et el. also discussed the presence of thermal gradient away from the centre of the sample [38], and advised in personal communication [94] that a slim rectangular design with less material to heat up is more optimal.

Unlike the dilatometry data shown above and in Sec. 4.1, which is used in the derivation of model parameters, the data collected by Di Ciano is not involved in the model derivation (except for the purpose of deriving priors as discussed in Sec. 5.3). This could provide a better illustration for the quantitative comparison since the models have not yet seen the data. Figure 33 shows a similar comparison of five repeats each at 1, 2, 5, and 10 K/s heating rate and the three model predictions.

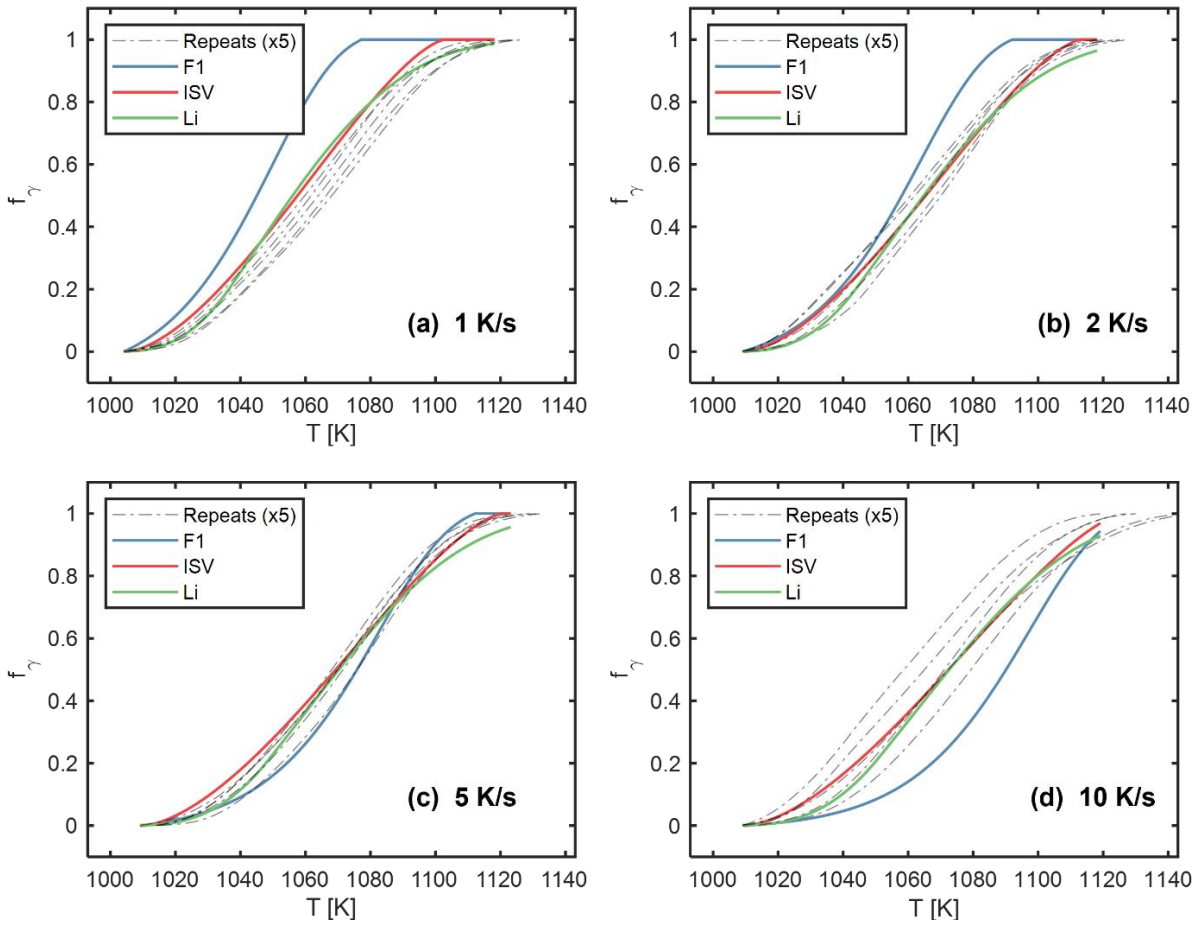

Figure 33: Qualitative comparison of dilatometry data by Di Ciano et al. [38] with the model prediction at different heating rates: (a) 1 K/s; (b) 2 K/s; (c) 5 K/s; and (d) 10 K/s

Similar observations can be made that F1 underperforms compared to the other two candidates, while the other two models appear to both perform well only based on qualitative goodness-of-fit. For heating rate 1, 2 and 5 K/s, both ISV and Li's model compares well against the five repeats. However, the runs for 10 K/s show higher than usual uncertainties, indicating some repeatability issue in the data, possibly due to the suboptimal sample shape discussed above.

6.2.Validation Against Datapaq Results

The selected candidate model, the ISV model, is integrated into the overall furnace model framework detailed in Sec. 3.1. The accuracy of the furnace model is validated using furnace trials run on the roller hearth furnace at Ford's facility. The blanks used for all trials are 1.6 mm thick, Usibor® 1500 with AS150 coating weight. The furnace parameters are summarized in Table 6.

Table 6: Furnace trials settings

Set-point [°C]	Trial (a)	Trial (b)
1	720	760
2	720	760
3	720	750
4	720	760
5	720	760
6	720	750
7	745	760
8	745	770
9	745	785
10	800	835
11	900	920
12	900	920
13	900	920
14	900	920
15	900	920
Roller Speed [m/s]	0.135	0.130

Two furnace trials are shown in Figure 34. The blanks are instrumented with Datapaq® units as shown in Figure 23 and sent through the furnace to collect the data. The blank temperature (TC) as it travels through the furnace is plotted against the model prediction (Model). The air temperature (T_{air}) collected by a TC probe is also shown. As discussed in Sec. 3.2, the model prediction is made based on the assumption that each furnace zone is large and isothermal, namely

its ambient temperature for convection, T_{amb} in Eq. (3-2), as well as surrounding temperature for radiation, T_{surr} in Eq. (3-8), all equal to the zone set-point. The ambient temperature (T_{amb}) is also plotted in both figures.

The different furnace heating zones (numbered 1 to 14) are marked at the top edge of the figure. Zone 15 is an ejection zone where the roller speed is increased to shoot the blank out of the furnace. Therefore, zone 15 does not show up on the plot since blank spends negligible time in this zone. The red marker denotes a physical baffle (three in total). Note that, ideally, each zone should be separated by baffles and able to maintain its own set-point without influence from other zones. In reality, there are only three baffles in this roller hearth furnace set-up, and the nearby zones will affect each other. In an attempt to account for this, the ambient temperatures are linearly interpolated if the neighboring zones have different set-points but have no baffles between them. For example, in Figure 34(a), the set-point for zone 9 and 10 are 1018 K and 1073K respectively. Due to the lack of baffle, zone 9 temperature starts at 1018 K and linearly increase to 1073 K. This linear profile, although imperfect, is generally validated by the trend shown in T_{air}. In both trials, T_{air} for the zones in between high and low set-point areas (approximately zone 8-10) show a gradual increase in temperature, rather than distinct uniform temperatures. Note that the sudden spike in T_{air} in Figure 34(b) is likely due to the TC probe accidentally hitting a tube burner inside the furnace and hence disregarded.

For both trials, the model prediction based on T_{amb} generally follows the trend of the TC data but consistently overpredicts the temperature. The difference is usually larger in the higher temperature zones and the transition between low to high set-point areas. One possible hypothesis is the furnace environment is not reaching the set-points, hence using set-points as model input (T_{amb}) would result in overprediction. Both trials show the measured air temperature, T_{air}, to be generally lower than the ambient temperature, T_{amb}, which is used by the model to make predictions and generated based on set-points and linear interpolations. This difference can range from 20 to as high as 90 K. Although the blank is irradiated by the furnace wall, and the air temperature can be lower than the wall temperature, a 20-90 K difference does provide some support for such hypothesis. A simple way to verify this is to use T_{air} as the model input instead of T_{amb}. The new predictions are shown as dashed curves in Figure 34. In both cases this results in much better agreement with the data, further supporting the hypothesis.

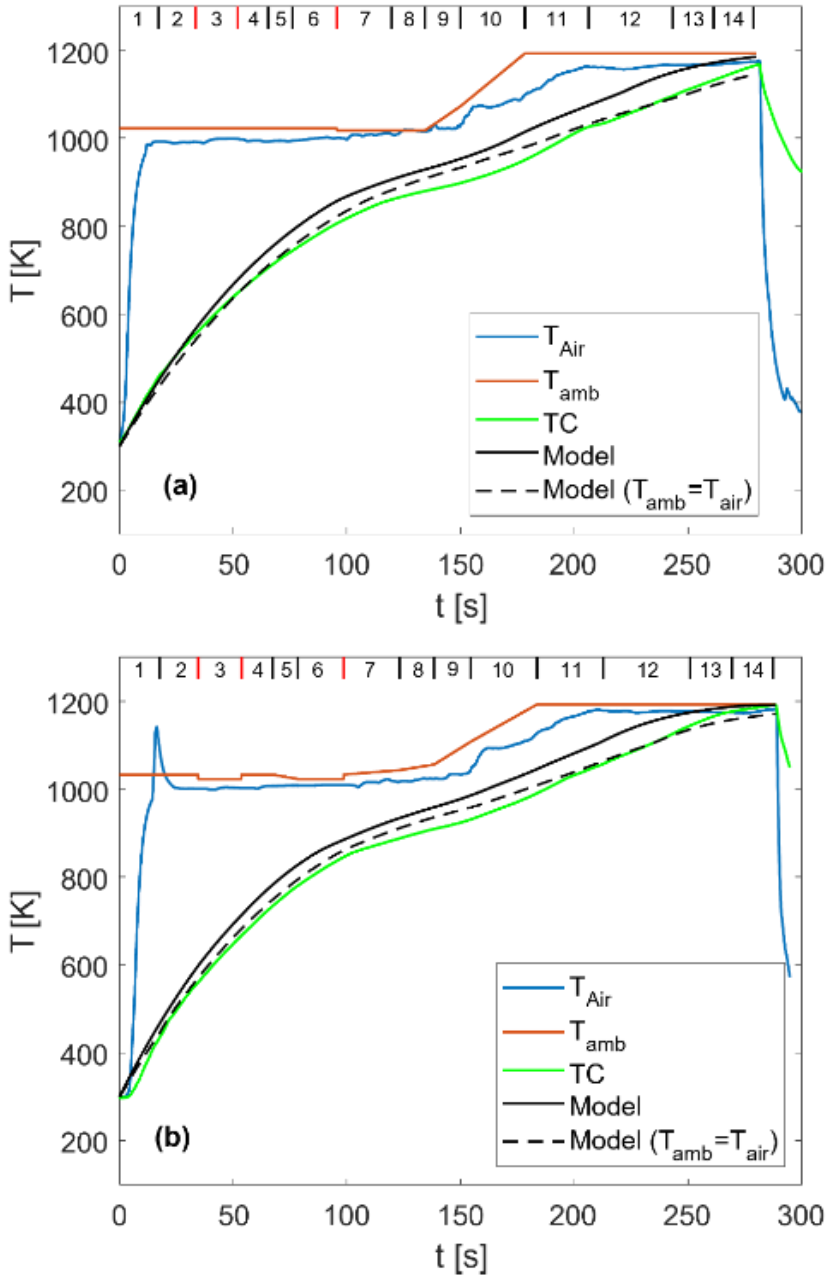

Figure 34: Two roller hearth furnace trials (a) and (b). The furnace zones are illustrated at the top and red markers denote physical baffles. T_{air} is the furnace air temperature measured by a TC probe attached to the blank. T_{amb} is the ambient temperature based on zone set-points, and is used as model input. The model prediction, and model prediction when using T_{air} as input are also shown.

Chapter 7 Conclusions and Future Work

7.1.Conclusions

The heating stage of the HFDQ process, typically done using a roller hearth furnace, is very time and energy intensive, and therefore has high potential for optimization. The conventional trial-and-error approach used to identify the process parameters rarely results in an optimal solution. This calls for a furnace model that can predict both the heating and austenitization aspect of the process and is also relatively simple to use. This work presents a model framework which combines a heat transfer submodel and an austenitization submodel. The heat transfer submodel considers natural convection, and radiative heating as the main source of energy input. It is also coupled with the austenitization submodel through the latent heat of austenitization.

When choosing an austenitization submodel, the challenge of how to select one of the many candidate models arises. The conventional goodness-of-fit model evaluation method does not consider the uncertainties in the data and the trade-off between model complexity and accuracy. Therefore, this work also establishes the procedure of applying Bayesian model selection to evaluate and select the austenitization submodels. Three candidate austenitization models are used to demonstrate this technique: the simple F1 model with two DOFs; a more complex ISV model with four DOFs; and a detailed phenomenological model with 10 DOFs that considers nucleation, growth, and impingement effect of austenitization. Dilatometry data is collected using a Gleeble 3500 thermomechanical simulator with a C-Gauge set-up. This data, along with additional dilatometry data from previous studies, provides the necessary information needed to quantify uncertainties in the experimental process and conduct the analysis. Through Bayesian model selection, it was quantitatively determined that the simplest F1 model lacks in accuracy, while the detailed 10 DOFs model does not bring enough improvements to justify its additional complexity. The ISV model best balances accuracy and complexity, and is therefore selected as the optimal option. The three austenitization models are also qualitatively compared against dilatometry data sets. This exercise further illustrates the need for Bayesian model selection technique, as the conventional goodness-of-fit comparison cannot effectively distinguish between ISV and phenomenological model.

The overall roller heath furnace model, with the optimal austenitization submodel, is then validated against two roller hearth furnace trials. The model shows promising results but consistently overpredicts the blank temperature when compared to the furnace trials. This is suspected to be caused by the furnace surrounding temperatures being lower than the corresponding zone set-points due to the lack of physical baffles between high and low temperature zones. This theory is tested by using the air temperature collected in the furnace trial as model input instead of furnace set-points, and this results in improved agreements between model prediction and TC data.

7.2.Future Work

This thermal-metallurgical model provides a useful tool for industrial engineers to study the heating process of hot stamping and improve its efficiency. The model can be extended to be applied in many applications. In addition, many aspects of the model can still be refined.

7.2.1.Potential Applications

The most immediate application for such thermometallurgical model is to be used as a diagnostic tool for industrial engineers designing the hot stamping process. In case of problems such as incomplete austenitization, this model can be used as a reference to examine the possible root cause and what process parameters need to be modified to address the issue.

This model can also be used to quickly iterate and refine new process parameters. The hot stamping production line often needs to accommodate a variety of blank thicknesses associated with component design changes. The conventional trial and error approach is inefficient, both in terms of the time it takes to obtain a new set of parameters and the suboptimality of the final outcome. Furthermore, the conventional approach requires production downtime, and will inevitably result in wasted material in the process. With a detailed furnace model, the process designer can quickly prototype a set of reasonable process parameters, before validating them on the production line. This greatly reduces the turnaround time for any production changes.

To take this one step further, with a model-based approach, one could also explore different numerical simulation techniques to come up with optimal process parameters that best balance the need of fully austenitizing the blank and improve energy efficiency.

7.2.2.Further Refinements

7.2.2.1.Quantification of Furnace Environment Uncertainties

The roller hearth furnace is controlled by a hysteresis scheme i.e., heaters turn on when the corresponding control TC input falls below the set-point and turns off when it exceeds the set-point. This relatively rudimentary control scheme causes fluctuation within the furnace environment, which in turn will cause fluctuation in the heating process. Consequently, one would expect differences in heating profile between different runs even with the same material and process parameters. So far, this study looks at the modelling problem from a deterministic approach with simplifying assumptions such as uniform zone temperatures. A more robust approach would be to look at the model from a probabilistic point of view and incorporate the uncertainties induced by the furnace fluctuation, such as the case in the work by Verma [37]. This way the model can not only produce a single prediction, but also an expected range given the uncertainties. The industrial engineers can make sure the process parameters are sufficient not only under the perfect condition but also the higher or lower end of the possible outcomes. To achieve this, one could instrument the key components within the furnace, including the radiant tube burners, the furnace walls, as well as measuring the air temperature with exposed TC probes. This experiment would likely record a cyclic response as the furnace heaters turn on and off, and the furnace environment overshoots and drops below the set-point as a result. This information will help quantify the uncertainties within the furnace, which can then be propagated into the model prediction to provide an average prediction associated with a possible upper and lower bound.

7.2.2.2.Examination on The Effect of Baffles

Further experimentation can also be conducted to better understand the effect of baffles. Neighboring zones can be instrumented to record the temperature data with or without baffles separating them. The experiment should be conducted with a wide range of temperature differences. One would expect that, were the neighboring zones to have similar set-points, the effect of physical sectioning is not substantial. On the contrary, if the adjacent zone set-point difference is large, the lack of baffle will likely cause larger fluctuation in zone temperatures, or in more extreme cases, the zones will not be able to maintain the set-point at all. In other words,

without a thermal barrier, the lower temperature zone will be constantly above the set-point under the influence of the higher temperature zone, while the higher temperature zone will struggle to achieve the set-point since it is effectively also heating up the neighboring zones. Due to cost constraints, not every zone in a roller hearth furnace can be baffled, such as the case for the roller hearth furnace set-up used in the present study. Therefore, understanding the effect of baffles will not only improve the accuracy of the furnace model, but also help determine the optimal baffle placements.

7.2.2.3. Improvements in Radiative Properties and Coating Evolution Modelling

The evolution of the Al-Si coating significant1 impacts the radiative properties, in ways that are not yet fully understood. Attempts have been made to quantify the change in radiative properties as detailed in Sec. 3.2.3, however, there is still room for improvements. The FTIR heated stage set-up introduced in Sec. 3.2.3 shows great potential but has key limitations. With those limitations addressed, one could measure in-situ emissivity as the material is being heated according to a furnace heating schedule to get a set of radiative properties that are more relevant to industrial applications. More studies could also be done on coating weights other than AS150 as their usage becomes more popular.

To take a more model-based approach, with further development in coating evolution modelling, one could also quantitatively connect the coating transformation with changes in radiative properties. The modular structure of the furnace model framework facilitates incorporation of new coating transformation submodels. This approach produces more accurate radiative properties without the need of extrapolations. The temperature prediction can also inform the coating transformation submodel, bringing the added benefit of more insights into how the process parameters might affect the coating transformation process. Since roller damage due to molten Al-Si coating is a problem yet to be addressed effectively, this coating submodel can provide a useful tool to design processes that not only maximizes efficiency but also mitigates roller pollution.

7.2.2.4. Additional Austenitization Candidate Submodels

In terms of austenitization model selection, the primary focus of this work is on the procedural derivation of the Bayesian model selection technique. Although a thorough literature review has

been conducted on different austenitization models, only three candidate models that best demonstrate the advantage of Bayesian model selection were compared. Future work could focus on a more thorough model comparison that includes more candidate models. With more development in the field, there are potentially newer and superior austenitization models as well. In addition to more models, the dilatometry data used for the derivation and selection process could also be improved. The Gleeble 3500 thermo-mechanical simulator is a very versatile tool capable of running a wide range of metallurgical experiments, and the C-Gauge attachment does allow it to measure width dilation of the sample. However, it is not a specialized dilatometer, therefore, it lacks in accuracy in some cases. More dilatometry experiments conducted in a specialized dilatometry will bring improvements to the model selection process as well.

References

[1] B. Zhao, T. A. Sipkens and K. J. Daun, "Choosing an optimal austenitization submodel using Bayesian model selection (under review)," *Metall. Mater. Trans. B.*

[2] H. Karbasian and A. Tekkaya, "A Review on Hot Stamping," *Journal of Materials Processing Technology,* vol. 210, no. 15, pp. 2103-2118, 2010.

[3] R. A. Turetta, S. Bruschi and A. Ghiotti, "Investigation of 22MnB5 Formability in Hot Stamping Operations," *Journal of Materials Processing Technology,* vol. 177, pp. 396-400, 2006.

[4] W. Joost, "Reducing Vehicle Weight and Improving US Energy Efficiency Using Integrated Computational Materials Engineering," *JOM,* vol. 64, no. 9, pp. 1032-1038, 2012.

[5] J. Aspacher, "Froming harderning concepts," in *1st International Conference on hot Sheet Metal Forming of High-Performance Steel*, Kassel, Germany, 2008.

[6] A. Hund, "Continuous Improvement of Hot Forming Technology," in *3rd International Conference on Sheet Metal Forming of High Performance Steel*, Kassel, Germany, 2011.

[7] N. Field, "Austenitization of Ultra High Strength Steel by DIrect Contact Heating for Hot Forming Die Quenching," *PhD Thesis, University of Waterloo*, 2017.

[8] M. Merklein and J. Lechler, "Investigation of the Thermo-Mechanical Properties of Hot Stamping Steels," *Journal of Materials Processing Technology*, vol. 177, pp. 452-455, 2006.

[9] C. Allély, L. Dosdat, O. Clauzeau, K. Ogle and P. Volovitch, "Anticorrosion Mechanisms of Aluminzied Steel for Hot Stamping," *Surface and Coating Technology,* vol. 238, pp. 188-196, 2014.

[10] C. Klassen and K. Daun, "Investigating coating liquefaction and solidification of furnace-heated Al-Si coated 22MnB5 steel using laser reflectance," *Surface & Coating Technology*, vol. 393, 2020.

[11] M. Windmann, A. Röttger and W. Theisen, "Phase Formation at The Interface Between a Boron Alloyed Steel Substrate and an Al-rich coating," *Surface and Coating Technology*, vol. 226, pp. 130-139, 2013.

[12] F. Borsetto, A. Ghiotti and S. Bruschi, "Investigation of The High Strength Steel Al-Si Coating During Hot Stamping Operations," *Key Engineering Materials*, vol. 410, pp. 289-296, 2009.

[13] H. Lehmann, "Developments in the field of Schwarz Heat Treatment Furnaces for Press Hardening Industry," in *3rd International Conference on Hot Sheet Metal Forming of High Performance Steel*, Kassel, Germany, 2011.

[14] M. G. Twynstra, K. J. Daun, E. Caron, N. Adam and F. Womack, "Modelling and Optimization of a Batch Furnace for Hot Stamping," in *ASME Summer Heat Transfer Conference* , Minneapolis, MN, 2013.

[15] B. A. Beherens, S. Hübner and M. Demir, "Conductive Heating System for Hot Sheet Metal Forming," in *1st International Conference on hot Sheet Metal Forming of High Performance Steel*, Kassel, Germany, 2008.

[16] V. Ploshhikin, A. Prihodovsky, J. Kaiser, H. Linder, C. Lengsdor and K. Roll, "New Heating Technology for the Furnace-Free Press Hardening Process," in *Tools and Technologies for Processing Ultra-High Strength Materials*, Graz, Austria, 2011.

[17] J. N. Rasera, K. J. Daun and M. d'Souza, "Direct Contact Heating for Hot Forming Die Quenching," in *ASME International Mechanical Engineering Congress and Exposition*, Montreal, QC, 2014.

[18] R. Kolleck, R. Veit, H. Hofmann and F. J. Lenze, "Alternative Heating Concepts for Hot Sheet Metal Forming," in *1st International Conference on hot SHeet Metal forming of High Performance Steel*, Kassel, Germany, 2008.

[19] K. S. Jhajj, "Heat Transfer Modeling of Roller Hearth and Muffle Furnace," *Master's Thesis, University of Waterloo*, 2015.

[20] M. Verma, H. Yan, J. Culham, M. Di Ciano, K. Daun and M. Verma, "Development and Validation of a Thermometallurgical Model for Funace-Based Austenitization During Hot Stamping," *Journal of Heat Transfer*, vol. 141, no. 6, p. 10, 2019.

[21] H. E. Pike Jr and S. J. Citron, "Optimization Studies of a Slab Reheating Furnace," *Automatica*, vol. 6, no. 1, pp. 41-50, 1970.

[22] H. Ramamurthy, S. Ramadhyani and R. Viskanta, "A Thermal System Model for a Radiant Tube Continuous Reheating Furnace," *Jounral of Materials Engineering and Performance*, vol. 4, no. 5, pp. 519-531, 1995.

[23] N. Charkraborti, K. Deb and A. Jha, "A Genetic Algorithm Based Heat Transfer Analysis of a Bloom Tr-heating Furnace," *Steel Research*, vol. 71, no. 10, pp. 396-402, 2000.

[24] S. H. Han, S. W. Baek and M. Y. Kim, "Transient Radiative HEating Characteriscis of Slabs in a Walking Beam Type Reheating Furnace," *International Journal of Heat and Mass Transfer*, vol. 52, no. 3-4, pp. 1005-1011, 2009.

[25] A. Steinboeck, D. Wild, T. Kiefer and A. Kugi, "A Mathematical Model of a Slab Reheating Furnace With Radiative Heat Transfer and Non-participating Gaseous Media," *International Journal of Heat and Mass Transfer* , vol. 53, no. 25-26, pp. 5933-5946, 2010.

[26] V. R. Heng, H. S. Ganesh, A. R. Dulaney, A. Kurzawski, M. Baldea, O. A. Ezekoye and T. F. Edgar, "Energy-oriented Modeling and Optimization of a Heat Treating Furnace," *Journal of Dynamic Systems, Measruement, and Control*, vol. 139, no. 6, 2017.

[27] S. R. Carvalho, T. H. Ong and G. Guimaraes, "A Mathematical and Computational Model of Furnces for Continuous Steel Strip Processing," *Jounrla of Material Processing Technology,* vol. 178, no. 1-3, pp. 179-387, 2006.

[28] W. Wu, Y. Feng and X. Zhang, "Zonal method solution of radiative heat transfer in a one-dimensional long roller-hearth furnace in CSP," *Jounral of Unviersity of Science and Technology Beijing, Mineral, Metallurgy, Material,* vol. 14, no. 4, pp. 307-311, 2007.

[29] Q. Gao, Y. Pang, Q. Sun, D. Liu and Z. Zhang, "Modeling approach and numerical analysis of a roller-hearth reheating furnace with radiant tubes and heating process optimization," *Case Studies in Thermal Engineering,* vol. 28, p. 101618, 2021.

[30] H. S. Ganesh, T. F. Edgar and M. Baldea, "Modeling, optimization and control of an austenitization furnace for achieving target product toughness and minimizing energy use," *J. Process Control,* vol. 74, pp. 177-188, 2019.

[31] D. F. Watt, L. Coon, M. Bibby, J. Goldak and C. Henwood, "An Algorithm for Modelling Microstructural Development in Weld Heat-affected Zones (Part A) Reaction Kinetics," *Acta Metallurgica,* vol. 36, no. 11, pp. 3029-3035, 1988.

[32] K. Morgan, R. W. Lewis and O. C. Zienkiewicz, "An Improved Algorithm for Heat Conduction Problems with Phase Change," *International Journal for Numerical Methods in Engineering,* vol. 12, no. 7, pp. 1191-1195, 1978.

[33] C. Bonacina, G. Comini, A. Fasano and M. Primicerio, "Numerical Solution of Phase-change Problems," *International Journal of Heat and Mass Transfer,* vol. 16, no. 10, pp. 1825-1832, 1973.

[34] M. Twynstra, K. Duan, E. Caron, N. Adam and D. Womack, "Modelling and Optimization of a Batch Furncae For Hot Stamping".

[35] G. P. Krielaart, C. M. Brakman and S. Van Der Zwaag, "Analysis of phase transformation in Fe-C alloys using differential scanning calorimetry," *Journal of Materials Science,* vol. 31, pp. 1501-1508, 1996.

[36] K. Jhajj, S. Slezak and K. Daun, "Inferring the Specific Heat of an Ultra High Strength Steel During the Heating Stage of Hot Forming Die Quenching, Through Inverse Analysis," *Applied Thermal Engineering,* vol. 83, pp. 98-107, 2015.

[37] M. Verma, "MASc thesis," *University of Waterloo,,* 2019.

[38] M. Di Ciano, N. Field, M. Wells and K. Daun, "Development of an Austenitization Kinetics Model for 22MnB5 Steel," *Journal of Materials Engineering and Performance,* vol. 27, no. 4, p. 1792, 2018.

[39] N. Li, J. Lin, D. Balint and T. Dean, "Modelling of Austenite Formation during Heating in Boron Steel Hot Stamping Processes," *Journal of Materials and Processing Technology*, vol. 237, pp. 394-401, 2016.

[40] X. Luo, L. Han and J. Gu, "Study on Austenitization Kinetics of SA508 Gr.3 Steel Based on Isoconversional Method," *Metals,* vol. 6, no. 1, p. 8, 2015.

[41] B. Zhao, C. Chiriac and K. J. Daun, "Evaluation of 22MnB5 Steel Austenitization Sub-Models for Simulating the Heating Phase of Hot Stamping," *2020 IOP Conf. Ser.: Mater. Sci. Eng.*, vol. 967, p. 012076.

[42] H. Huang, B. Wang, X. Tang and J. Li, "Modeling of Non-isothermal Austenite Formation in Spring Steel," *Metall. Mater. Trans. A*, vol. 48, pp. 5799-5804, 2017.

[43] R. Dutta, M. Bogdan and J. k. Ghosh, "Model Selection and Multiple Testing - A Bayesian and Empirical Bayes Overview and some New Results," *JISA*, vol. 50, pp. 105-142, 2012.

[44] A. E. Raftery, "Bayesian Model Selection in Social Research," *Sociological Methodology*, vol. 25, pp. 111-163, 1995.

[45] S. H. Cheung, T. A. Oliver, E. E. Prudencio, S. Prudhomme and R. D. Moser, "Bayesian uncertainty analysis with applications to turbulence modeling," *Reliab. Eng. Syst. Saf.*, vol. 96, no. 9, pp. 1137-1149, 2011.

[46] R. Trotta, "Applications of Bayesian Model Selection to Cosmological Parameters," *Monthly Notices of the Royal Astronomical Society,* vol. 378, no. 1, pp. 72-82, 2007.

[47] T. A. Sipkens, P. J. Hadwin, S. J. Grauer and K. J. Daun, "Predicting the heat of vaporization of iron at high temperatures using timeresolved laser-induced incandescence and Bayesian model selection," *J. Appl. Phys.,* no. 123, p. 095103, 2018.

[48] M. Naderi, "Hot Stamping of Ultra High Strength Steels," *MASc Thesis, RWTH Aachen University,* 2007.

[49] C. Chiriac and R. Sohmshetty, "The Effects of the Heating Rate and the Incoming Microstructure on Phase Transformation Temperatures of 22MnB5 Steel," in *CHS2*, 2017.

[50] M. Naderi, A. Saeed-Akbari and W. Bleck, "The Effects of Non-isothermal Deformation on Martensitic Transformation In 22MnB5 Steel," *Materials Science and Engineering A,* vol. 487, no. 1-2, pp. 445-455, 2008.

[51] F. G. Caballero, C. Capdevila and C. G. De Andres, "Modelling of Kinetics and Dilatometric Behaviour of Austenite Formation in a Low-carbon Steel With a Ferrrite Plus Pearlite Initial Microstrucutre," *Journal of Material Science,* vol. 37, no. 16, pp. 3533-3540, 2002.

[52] J. N. Rasera, K. J. Daun, C. J. Shi and M. D'Souza, "Direct contact heating for hot forming die quenching," *Applied Thermal Engineering,* vol. 98, pp. 1165-1173, 2016.

[53] N. Li, J. Lin, D. S. Balint and T. A. Dean, "Experimental characterisation of the effects of thermal conditions on austenite formation for hot stamping of boron steel," *Journal of Materials Processing Technology* , vol. 231, pp. 254-264, 2016.

[54] M. A. Asadabad, M. Goodarzi and S. Kheirandish, "Kinetics of Austenite Formation in Dual Phase Steels," *ISIJ International,* vol. 48, no. 9, pp. 1251-1255, 2008.

[55] F. Oliveira, M. S. Andrade and A. B. Cota, "Kinetics of austenite formation during continuous heating in a low carbon steel," *Materials Characterization,* vol. 58, no. 3, pp. 256-261, 2007.

[56] J. Cai, "Modelling of Phase Transformation in Hot Stamping of Boron Steel, PhD Thesis," *Imperial College London, England,* 2011.

[57] D. Askeland, P. Fulay and W. Wright, The Science and Engineering of Materials 6th Ed, Global Engineering, 2010.

[58] H. K. Khaira, A. K. Jena and M. C. Chaturvedi, "Effects of heat treatment cycle on equilibrium between ferrite and austenite during intercritical annealing," *Materials Science and Engineering: A,* vol. 161, no. 2, pp. 267-271, 1993.

[59] G. R. Speich, V. A. Demarest and R. L. Miller, "Formation of Austenite During Intercritical Annealing of Dual-Phase Steels," *Metall. Mater. Trans. A ,* vol. 12, pp. 1419-1428, 1981.

[60] J. Huang, W. Poole and M. Militzer, "Austenite Formation During Intercritical Annealing," *Metallurgical and Materials Transactions A,* vol. 35, pp. 3364-3375, 2004.

[61] G. A. Roberts and R. F. Mehl, "The Mechanism and the Rate of Formation of Austenite from Ferrite-cementite Aggregates," *Transactions of the ASM,* vol. 31, pp. 613-650, 1943.

[62] F. G. Caballero, C. Capdevila and C. García de Andrés, "Influence of scale parameters of pearlite on the kinetics of anisothermal pearlite to austenite transformation in a eutectoid steel," *Scripta Materialia,* vol. 42, no. 12, pp. 1159-1165, 2000.

[63] A. Roósz, Z. Gácsi and E. G. Fuchs, "Isothermal formation of austenite in eutectoid plain carbon steel," *Acta metall.,* vol. 31, no. 4, pp. 509-517, 1983.

[64] V. I. Savran, Y. Van Leeuwen, D. N. Hanlon, C. Kwakernaak, W. G. Sloof and J. Sietsma, "Microstructural Features of Austenite Formation in C35 and C45 alloys," *Metallurgical and materials Transacctions A,* vol. 38, pp. 946-955, 2007.

[65] A. Jacot and M. Rappaz, "A combined model for the description of austenitization, homogenization and grain growth in hypoeutectoid Fe–C steels during heating," *Acta Materialia,* vol. 47, no. 5, pp. 1645-1651, 1999.

[66] D. P. Datta and A. M. Gokhale, "Austenitization Kinetics of Pearlite and Ferrite Aggregates in a Low Carbon Steel Containing 0.15 wt pct C," *Metallurgical Transactions A,* vol. 12, no. 3, pp. 443-450, 1981.

[67] J. J. Yi, I. S. Kim and H. S. Choi, "Austenitization during intercritical annealing of an Fe–C–Si–Mn dual-phase steel," *Metallurgical Transactions A,* vol. 16, no. 7, pp. 1237-1245, 1985.

[68] C. García De Andrés, F. G. Caballero, C. Capdevila and L. F. Álvarez, "Application of dilatometric analysis to the study of solid-solid phase transformations in steels," *Materials Characterization,* vol. 48, no. 1, pp. 101-111, 2002.

[69] ArcelorMittal, "Steels coated with Alusi, an aluminium-silicon alloy," [Online]. Available: https://automotive.arcelormittal.com/products/flat/coatings/alusi. [Accessed 26 Feb 2022].

[70] C. M. Klassen, J. Emmert and K. J. Daun, "Effect of Coating Thickness on the in-situ Reflectance and Surface Roughness of Al-Si Coated 22MnB5 Steel," *Surface and Coating Technology,* vol. 414, p. 127100, 2021.

[71] R. Grigorieva, P. Drillet, J. M. Mataigne and A. Redjaïmia, "Phase transformations in the Al-Si coating during the austenitization step," *Solid State Phenomena,* Vols. 172-174, pp. 784-790, 2011.

[72] L. Pelcastre, J. Hardell, A. Rolland and B. Prakash, "Influence of microstructural evolution of Al-Si coated UHSS on its tribological behaviour against tool steel at elevated temperatures," *Journal of Materials Processing Technology,* vol. 228, pp. 117-124, 2016.

[73] Z. Gui, W. Liang and Y. Zhang, "Enhancing ductility of the Al-Si coating on hot stamping steel by controlling the Fe-Al phase transformation during austenitization," *Science China Technological Sciences,* vol. 57, pp. 1785-1793, 2014.

[74] M. Kolaříková, R. Chotěborský, M. Hromasová and M. Linda, "The Characteristics of AlSi Coating on Steel 22MnB5 Depending on the Heat Treatment," *Acta Polytechnica,* vol. 59, no. 4, pp. 351-357, 2019.

[75] D. W. Fan and B. C. De Cooman, "State-of-the-Knowledge on Coating Systems for Hot Stamped Parts," *Steel Research International* , vol. 83, no. 5, pp. 412-433, 2012.

[76] F. Jenner, M. E. Walter, R. M. Iyengar and R. Hughes, "Evolution of Phases, Microstructure, and Surface Roughness during Heat Treatment of Aluminized Low Carbon Steel," *Metallurgical and Materials Transactions A,* vol. 41, pp. 1554-1563, 2010.

[77] S. J. Grauer, E. Caron, N. L. Chester, M. A. Wells and K. J. Daun, "Investigation of Melting in the Al-Si Coating of a Boron Steel SHeet by Differential Scanning Calorimetry," *Journal of Materials Processing Technology* , vol. 216, pp. 89-94, 2015.

[78] C. Shi, K. J. Daun and M. A. Wells, "Spectral Emissivity Characteristics of the Usibor 1500P Steel During Austenitization In Argon and Air Atmospheres," *International Journal of Heat and Mass Transfer,* vol. 91, pp. 818-828, 2015.

[79] M. Barreau. et al, "In situ surface imaging: High temperature environmental SEM study of the surface changes during heat treatment of an Al-Si coated boron steel," *Materials Characterization,* vol. 163, 2020.

[80] M. Jönsson, "The Problem with Melted Al-Si in the Hot Stamping Furnace," in *The 3rd International Conference on Advanced High Strength Steel and Press Hardening*, Xi'an, 2017.

[81] T. Bergman, A. Lavine and D. Dewitt, Fundamentals of Heat and Mass Transfer, 6th ed., Hoboken, NJ.: Wiley, 2011.

[82] ArcelorMittal, "Properties of Usibor 1500P".

[83] C. Shi, K. Daun and M. Wells, "Evolution of the Spectral Emissivity and Phase Transformations of the Al-Si Coating on Usibor 1500P Steel During Austenitization," *Metallurgical and Materials Transactions,* vol. 47B, pp. 3301-3309, 2016.

[84] W. A. Johnson and R. F. Mehl, *Trans. Am. Inst. Min. (Metall.) Engs.,* vol. 135, p. 416, 1939.

[85] M. Avrami, "Kinetics of phase change. I: General theory," *J. Chem. Phys.,* vol. 7, no. 12, pp. 1103-1112, 1939.

[86] K. J. Laidler, "The Development of the Arrhenius Equation," *J. Chem. Educ.,* vol. 61, pp. 494-498, 1984.

[87] D. W. Henderson, "Thermal analysis of non-isothermal crystallization kinetics in glass forming liquids," *J. Non-Cryst. Solids.,* vol. 30, no. 3, pp. 301-315, 1979.

[88] Ø. Grong and H. R. Shercliff, "Microstructural Modelling in Metals Processing," *Prog. Mater. Sci.,* vol. 47, pp. 163-282, 2006.

[89] "Standard Test Method for Determining Volume Fraction by Systematic Manual Point Count," *ASTM E562 - 11. (n.d.).*

[90] E. T. Jaynes, "Prior Probabilities," *IEEE Trans Cybern,* vol. 4, no. 3, pp. 227-241, 1968.

[91] U. Von Toussaint, "Bayesian inference in physics," *Rev. Mod. Phys.,* vol. 83, pp. 943-999, 2011.

[92] R. E. Kass and A. E. Raftery, "Bayes factors," *JASA,* vol. 90, no. 430, pp. 773-795, 1995.

[93] S. J. Grauer, P. J. Hadwin, T. A. Sipkens and K. J. Daun, "Measurement-based meshing, basis selection, and prior assignment in chemical species tomography," *Opt. Express,* vol. 25, no. 21, pp. 25135-25148, 2017.

[94] M. Di Ciano, Interviewee, *Discussions about dilatometry experiment design for 22MnB5 Steel.* [Interview]. 21 03 2021.

[95] B. Zhu, Y. Zhang, C. Wang, P. Liu, W. Liang and J. Li, "Modeling of the Austenitization of Ultra-high Strength Steel with Cellular Automation Method," *Metallurgical and Materials Transactions,* Vols. A-45, pp. 3161-3171, 2014.

[96] H. Yan, M. Di Ciano, M. Verma and K. Daun, "Intercritical Annealing of 22MnB5 for Hot Forming Die Quenching," in *International Deep Drawing Research Group 37th Annual Conference*, Waterloo, ON, Canada, 2018, June 3-7.

[97] A. Panesar, D. Brackett, I. Ashcroft and et al, "Hierarchical remeshing strategies with mesh mapping for topology optimisations," *Int. J. Numer. Methods Eng.*, vol. 111, no. 7, pp. 676-700, 2017.

[98] A. Khawam and D. Flanagan, "Solid-State Kinetics Models: Basics and Mathematical Fundamentals," *J. Phys. Chem. B,* vol. 110, pp. 17315-17328, 2006.

[99] M. Güler, "Magnetism and Microstructure Characterization of Phase Transitions in a Steel," *Advances in Condensed Matter Physics*, vol. 2014, p. 4, 2014.

[100] F. Caballero, C. Capdevila and C. García de Andrés, "Influence of Pearlite Morphology and Heating Rate on the Kinetics of Continuously Heated Austenite Formation in a Eutectoid Stee," *Metall. Mater. Trans. A,* vol. 32A, pp. 1283-1291, 2001.

[101] M. J. Holzweißig, A. Andreiev, M. Schaper, J. Lackmann, S. Konrad, C. J. Rüsing and T. Niendorf, "Influence of Short Austenitization Treatments on the Mechanical Properties of Low Alloy Carbon Steel," in *5th International Conference on Hot Sheet Metal Forming of High Performance Steel*, Toronto, Canada, 2015.

Appendix A

Thermophysical properties of PHS1500 provided by the manufacturer [82]

Temperature [°C]	Conductivity [W/(m·K)]	Density [kg/m^3]	Specific Heat [J/(kg·K)]
0	38.6	7880.8	433
50	38.9	7864.5	444
100	39.5	7848.0	465
150	39.9	7831.5	485
200	40.4	7814.8	505
250	41.0	7797.7	525
300	40.7	7781.0	547
350	40.9	7763.9	571
400	40.6	7746.6	598
450	40.1	7729.2	628
500	39.5	7711.7	628
550	38.5	7694.0	701
600	37.4	7676.2	748
650	35.9	7658.3	804
700	34.4	7640.2	876
725	37.4	7631.1	924
750	40.3	7622.0	971
800	39.7	7603.7	942
850	25.1	7585.2	825
880	26.0	7574.0	793
900	26.6	7566.6	771
950	27.3	7567.0	741
1000	27.9	7567.0	723
1050	28.3	7567.0	711
1100	28.6	7567.0	706
1150	29.2	7567.0	706
1200	29.7	7567.0	706